

Electromagnetic Monitoring of Hydraulic Fracturing: Relationship to Permeability, Seismicity, and Stress

Stephan Thiel^{1,2} 

Received: 7 December 2016 / Accepted: 11 September 2017
© Springer Science+Business Media B.V. 2017

Abstract Hydraulic fracturing is a geoen지니어링 application designed to enhance sub-surface permeability to maximize fluid and gas flow. Fracking is commonly used in enhanced geothermal systems (EGS), tight shale gas, and coal seam gas (CSG) plays and in CO₂ storage scenarios. Common monitoring methods include microseismics and mapping small earthquakes with great resolution associated with fracture opening at reservoir depth. Recently, electromagnetic (EM) methods have been employed in the field to provide an alternative way of direct detection of fluids as they are pumped in the ground. Surface magnetotelluric (MT) measurements across EGS show subtle yet detectable changes during fracking derived from time-lapse MT deployments. Changes are directional and are predominantly aligned with current stress field, dictating preferential fracture orientation, supported by microseismic monitoring of frack-related earthquakes. Modeling studies prior to the injection are crucial for survey design and feasibility of monitoring fracks. In particular, knowledge of sediment thickness plays a fundamental role in resolving subtle changes. Numerical forward modeling studies clearly favor some form of downhole measurement to enhance sensitivity; however, these have yet to be conclusively demonstrated in the field. Nevertheless, real surface-based monitoring examples do not necessarily replicate the expected magnitude of change derived from forward modeling and are larger than expected in some cases from EGS and CSG systems. It appears the injected fluid volume alone cannot account for the surface change in resistivity, but connectedness of pore space is also significantly enhanced and nonlinear. Recent numerical studies emphasize the importance of percolation threshold of the fracture network on both electrical resistivity and permeability, which may play an important role in accounting for temporal changes in surface EM measurements during hydraulic fracturing.

✉ Stephan Thiel
stephan.thiel@sa.gov.au

¹ Geological Survey of South Australia, 4/101 Grenfell Street, Adelaide, SA 5000, Australia

² School of Physical Sciences, The University of Adelaide, Adelaide, SA 5005, Australia

Keywords Hydraulic fracking · Electromagnetic monitoring · Magnetotellurics · Permeability · Stress

1 Introduction

Energy production is vital for humanity as a whole, and demand is met by harvesting fossil and renewable energy fuels. A subset of the energy sources including geothermal and some forms of hydrocarbons, such as coal seam gas and shale gas resources, require geoengineering applications to unlock their potential. Both require a fluid to penetrate the formation in order to absorb the thermal energy, which can then be extracted at the surface for electricity generation or direct heating (geothermal), or to increase the permeability of the tight system to release methane to the surface. While these operations are widespread for gas production, particularly in the USA and Australia, geothermal plays rely on conventional geothermal systems, in which fluids already exist in the subsurface under high pressure. As a result, these geothermal systems can be drilled into and fluids will continue to advance to the surface for energy harvesting. Recently, a second model of enhanced geothermal systems has been tried for which fluids have to be injected to depths of a hot dry rock environment with elevated temperatures of around 200 °C at 4 km depth (Fig. 1). The injection of fluid and increase in permeability of the target formation are commonly referred to as hydraulic fracking, hydraulic fracturing or hydraulic stimulation.

Hydraulic fracking is a process in which fluids are pumped from the surface down a borehole under high pressure to create fractures in the rock matrix (Gérard et al. 2006). Fracking is employed in geothermal plays, specifically in enhanced geothermal systems (EGS), as conventional geothermal systems, such as those found in New Zealand and

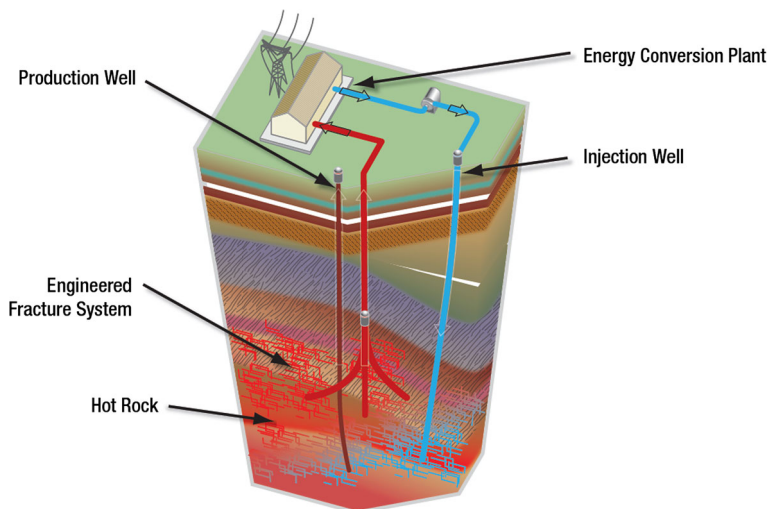


Fig. 1 Schematic diagram depicting an enhanced geothermal system (EGS) setup. Fluids are pumped at depth of typically around 4 km under high pressure to cause an enhanced fracture network susceptible to fluid flow. Once a permeable fractured network is established, the heated fluids are pumped back to the surface through a second borehole to generate electricity from a power plant. Used fluids are then reintroduced to hot rocks at depth. Adapted from Geothermal Technologies Program (2008)

Iceland (Bertrand et al. 2013; Heise et al. 2010; Árnason et al. 2010), do not typically require stimulation to achieve sufficient fluid flow (Genter et al. 2003). Ultimately, the success of enhanced geothermal areas depends on sufficient flow of fluid through the rock formation, for example from the injecting to producing drill hole. The hydraulic flow is primarily dependent on the permeability of the formation. In enhanced geothermal systems, the primary permeability, the interconnected pore space of the compacted, porous sedimentary rock, is typically not sufficient to enable commercially viable flow rates. Therefore, the introduction of fluids under pressure generates secondary permeability through establishment of faults and fractures (Muñoz 2014). Recent examples of EGS are at Soultz-sous-Forêt EGS (Gérard et al. 2006; Vogt et al. 2012), Paralana (Peacock et al. 2012, 2013; MacFarlane et al. 2014; Rosas-Carbajal et al. 2015), Habanero (Didana et al. 2017), and Rittershofen (Abdelfettah et al. 2018).

Another use of fracking is for release of tight shale gas (TSG) and coal seam gas (CSG) out of tight (close to impermeable) formations. The natural gas is predominantly methane, which is bound in shales between 1500 and 4500 m depth (Rees et al. 2016c; He et al. 2015; Rees et al. 2016b). Methane is trapped in coal seams at typically a few hundreds of meters depth. Initial pumping of fluid to depths with pressures higher than the in situ formation pressure establishes a fracture network of enhanced permeability, followed by extraction of injected and formation fluids. As a result, the host rock has enhanced permeability and reduced fluid content, allowing the natural gas in the shale or coal seams to escape via fractured pathways and borehole to the surface.

Microseismic monitoring has commonly been employed to map deformation associated with hydraulic fracking since the 1970s (Pearson 1981). The microseismic patterns are rarely diffuse but show distinct geometric patterns. As an example, in granite and massive, brittle sediments the seismicity shows a network of fractures (Albaric et al. 2014). The development of seismicity within a reservoir is therefore a proxy for higher permeability (Phillips et al. 2002). Stress due to the injection fluid decreases away from the drillhole derived from P-wave spectra, suggesting a decrease in pore pressure perturbation (Goertz-Allmann et al. 2011).

Electromagnetic methods, on the other hand, are typically used to characterize the subsurface of a geothermal or hydrocarbon area. Geothermal systems can be divided into three main types (Muñoz 2014). The most common are convective hydrothermal systems (Harinarayana et al. 2006; Bertrand et al. 2013; Garg et al. 2007; Heise et al. 2008), partial melt systems (Didana et al. 2015; Miensopust et al. 2014; Aizawa et al. 2009), and enhanced geothermal systems in hot dry rock environments (Liddell et al. 2016; Kirkby et al. 2015; Didana et al. 2017; MacFarlane et al. 2014). Conceptual models exist for the first two magmatically driven types. Hydrothermal systems are characterized by a heat source, a convective circulating fluid system beneath an impermeable clay cap. The lower-temperature (< 150 °C) illite–smectite clay alteration products are more electrically conductive than their higher temperature (200–240 °C) chlorite–epidote clay counterparts due to loosely bound cations in illite and smectite (Leroy and Revil 2004; Muñoz 2014; Kristinsdóttir et al. 2010). The hydrothermal fluid cell usually sits below the clay cap and breaks in the clay cap may lead to fluids propagating closer to the surface, resulting in self-potential field anomalies (Aizawa et al. 2009). Partial melts significantly reduce electrical resistivity by orders of magnitude compared to the dry rock equivalent (Pommier 2014), which makes electromagnetic measurements an ideal tool to map partial melts in the crust and provide constraints on the geometry of the geothermal system (Didana et al. 2014; Miensopust et al. 2014).

There exist no distinct physical properties for geophysical detection based on a conceptual model for enhanced geothermal systems in the same way as for magmatically driven conventional geothermal systems. EGS have a higher than normal temperature gradient with depth to achieve target temperatures of $\sim 200^\circ\text{C}$ at around 4 km depth. The source of the heat for EGS is non-magmatic and is the result of high-heat-producing granites enriched in radioactive elements (Genter et al. 2003). The system requires a heat trap in form of a sedimentary layer overlying the granites. The electrical resistivity of the basement is usually much higher than the overlying sedimentary layer, and depth to basement is well constrained with electromagnetic methods. The second important parameter for successful EGS operation, the permeability of the subsurface, is not as straightforward to determine from surface geophysical measurements (Spichak and Manzella 2009). Inverse models based on electromagnetic data are ambiguous, and joint inversion approaches seek to minimize ambiguity in the model space (Muñoz et al. 2010b; Moorkamp 2017; Bauer et al. 2012).

Characterization of hydrocarbon plays involves a combination of controlled-source electromagnetic (CSEM) methods and MT (Streich 2016). Most of the focus has been on hydrocarbons in the marine environment in search of thin and electrically resistive hydrocarbon layers. In this case, MT provides the background resistivity distribution and CSEM is used for direct targeting of the thin resistive layer, due to its superior sensitivity to resistors compared to MT (Constable and Weiss 2006; Weidelt 2007; Constable et al. 2009; Commer and Newman 2009). In recent years, an increasing number of modeling studies investigated the use of CSEM for CO_2 storage, e.g., around the Ketzin CO_2 storage formation (Grayver et al. 2014), with particular focus on modeling and sensitivity studies (Streich and Becken 2011; Streich et al. 2010).

Electromagnetic monitoring is becoming increasingly popular, including MT monitoring of hydraulic fracturing of enhanced geothermal reservoirs (Peacock et al. 2012, 2013; Abdelfettah et al. 2018), MT monitoring of hydrocarbon gas fracks (Orange et al. 2009; Rees et al. 2016a, b, c), DC resistivity and CSEM monitoring of CO_2 -sequestration scenarios (Streich et al. 2010; Börner et al. 2015a, b; Streich 2016), and CSEM monitoring of reservoir oil saturation using a borehole–surface configuration (Tietze et al. 2015). The motivation for using electromagnetic methods for fluid fracturing is the low resistivity of fluids compared to granitic or compacted sedimentary host rocks. An injection of a volume of fluid will result in a connected network at depth leading to a reduction in bulk electrical resistivity, which may be measurable using surface or borehole EM methods. The depth of the injection for the cases considered in this review is a few hundred meters to several kilometers depth. This requires lower-frequency EM methods such as MT to penetrate to target depths (Cagniard 1953; Tikhonov 1950). The period ($T = \frac{1}{f}$ in s) dependency of MT obeys the skin-depth relationship (Chave and Jones 2012):

$$\delta = 503\sqrt{\varrho T} \quad (1)$$

This relationship means it is possible to convert the period T to depth $\delta[\text{m}]$ given a resistivity ϱ in Ωm of the half-space below the measurement site. Conceptually, if there is a change in the responses for a particular period as a result of a fluid injection, the skin-depth relationship allows a conversion to depth. In the field, MT measures time-varying electric E and magnetic H field variations which are converted into the frequency domain. Both fields are related via the impedance tensor Z , a frequency-dependent transfer function describing the resistivity structure of the earth:

$$\begin{bmatrix} E_x \\ E_y \end{bmatrix} = \begin{bmatrix} Z_{xx} & Z_{xy} \\ Z_{yx} & Z_{yy} \end{bmatrix} \cdot \begin{bmatrix} H_x \\ H_y \end{bmatrix} \quad (2)$$

Each of the four elements of the complex impedance tensor may be expressed as an apparent resistivity ϱ_a :

$$\varrho_{a_{ij}}(\omega) = \frac{1}{\mu\omega} |Z_{ij}(\omega)|^2, \quad (3)$$

and phase ϕ defined as the ratio of the imaginary (\Im) to the real (\Re) part of Z :

$$\phi_{ij}(\omega) = \tan^{-1} \left(\frac{\Im Z_{ij}}{\Re Z_{ij}} \right) \quad (4)$$

While microseismic monitoring maps rock failure due to the stresses applied by the fluid injection, EM monitoring is directly sensitive to the injected fluids due to their much lower electrical resistivity compared to the host rocks (Nesbitt 1993).

Previous related workshop reviews have concentrated on electromagnetic field monitoring of seismic and volcanic activities (Uyeshima 2007), EM monitoring for hydraulic studies (Slater 2007), and land-based CSEM studies (Streich 2016). This review expands on the plethora of previous work by illuminating deep-seated, human-induced fluid injections requiring lower-frequency EM measurements. I will discuss the challenges due to the low sensitivity of the deep-probing electromagnetic methods to the deep target depths of fluid fracking and show approaches to allow for robust estimation of response function changes as well as ways to convert the changes into the model domain. The manuscript will then cover the field examples that have been studied over the recent years, mostly on the Australian continent, but with a few examples in other parts of the world. I will then digress to introduce permeability as the crucial parameter for understanding fluid flow at depth from both laboratory measurements and recent developments in linking these laboratory results to field observations.

2 Sensitivity of EM Monitoring to Hydraulic Fracking

In its simplest sense, electromagnetic monitoring of fluid fracking implies the detection of changes in apparent resistivity ϱ_a and phase ϕ during the event. It is therefore a requirement to compare EM responses measured during fracking with a baseline data set acquired before the underground frack commenced. The survey layout for time-lapse deployment is typically small and less than 20 km in extent. The influence of local noise may lead to biased estimates of local transfer functions in case of strong resistivity contrasts (Muñoz and Ritter 2013). Computing inter-station transfer functions may help to circumvent this problem, as shown in the case of the Schönebeck geothermal test site, Germany (Muñoz and Ritter 2013).

Ideally, modeling studies should precede field deployments for monitoring to optimize survey design and verify the feasibility of the survey. It is crucial to populate the model domain with a realistic resistivity distribution of the injection site to ensure optimal prediction. Common approaches include a prior MT field study (Peacock et al. 2012; Didana et al. 2017) to obtain an inverse model derived from resistivity distribution, or using existing 3D geological models with assigned resistivity values to lithological units (Börner et al. 2015a). The former approach is advantageous, as laboratory-derived resistivity values typically represent an average value and quite often do not account for minor

conducting phases, nor do they adequately take the dimensionality of the subsurface into account (Ogaya et al. 2016).

2.1 Screening Effect of Sedimentary Cover

One of the main challenges for EM monitoring of hydraulic fracking is the large target depth, ranging from few hundreds of meters to several kilometers depth. The majority of field examples to date illustrate that changes in the EM responses are barely larger than noise levels during a time-lapse deployment of EM receivers such as MT or CSEM. The test cases on geothermal and unconventional plays of the Australian continent, for example, show a common lithological stratification with an electrically conductive sedimentary layer overlying resistive basement (Peacock et al. 2012; Rees et al. 2016c; Kirkby et al. 2015). Thickness of the conductive sedimentary layers exceeds a few hundred meters in most cases. The resistivity of the sediments is largely controlled by the porosity φ and the conductivity of the fluid σ_f . The fluid conductivity increases with depth z , starting from a surface temperature T_0 and surficial fluid conductivity σ_0 (Nesbitt 1993):

$$\sigma_f = \sigma_0 \frac{T_0 + z\delta T}{10}. \quad (5)$$

At the same time, porosity can often be modeled by an exponential decrease (with depth z a negative number) (Athys 1930):

$$\varphi = \varphi_0 e^{\alpha z}. \quad (6)$$

As a result, the bulk resistivity of the sediments is relatively constant for the sedimentary package in the top few kilometers (Fig. 2), and deviations are often due to other minor

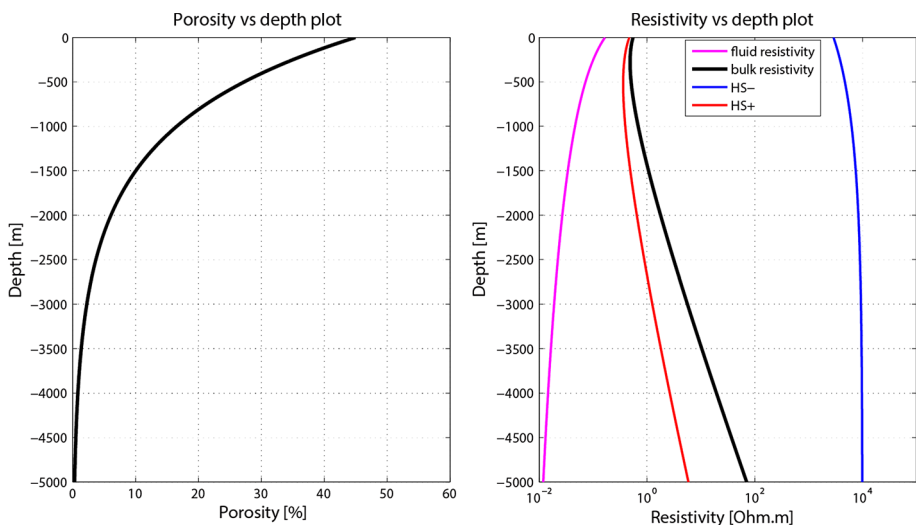


Fig. 2 Sediment porosity as a function of depth (left) and the resulting range of bulk and fluid resistivity with depth (right). The bulk resistivity is derived from Archie's law (Eq. 13) for maximum (Hashin-Shtrikman bounds, HS+) and minimum (HS-) connected media (Hashin and Shtrikman 1962). The values are approximate for the Paralana EGS with a surface porosity $\varphi = 45\%$, a surface fluid conductivity of $\sigma_f = 3 \text{ S/m}$, a mineral grain conductivity of $\sigma_s = 10^{-4} \text{ S/m}$, a geothermal gradient of $\Delta T = 52 \text{ }^\circ\text{C/km}$, and a cementation factor of 1.5

conducting phases, such as clay layers. It should be noted that the relationships described in Eqs. 5 and 6 are more or less simplified and are a good approximation for sedimentary packages below about 200 °C. The example in Fig. 2 was modeled based on parameters applicable to the Paralana EGS with a surface fluid conductivity of $\sigma_f = 3 \text{ S/m}$, a mineral grain conductivity of $\sigma_s = 10^{-4} \text{ S/m}$, a geothermal gradient of $\Delta T = 52 \text{ }^\circ\text{C/km}$, a cementation factor m of 1.5, and an assumed surface porosity of $\varphi = 45\%$. The surface porosity in this study is relatively high for soils and sediments, with values typically around 35–45% (Chesworth 2008). Using Eqs. 5 and 6, the modeled bulk resistivity is between less than $1 \text{ } \Omega \text{ m}$ near the surface and $100 \text{ } \Omega \text{ m}$ at depths of 5 km (Fig. 2) using an estimation based on Archie's equation (see Sect. 4.1) (Archie 1942):

$$\sigma = \sigma_s + (\sigma_f - \sigma_s)\varphi^m \quad (7)$$

The Hashin–Shtrikman upper (HS+) and lower (HS–) bounds are plotted for comparison, and it becomes clear that Archie's law sits much closer to the HS+ bounds than the HS– bounds (Hashin and Shtrikman 1962). The Hashin–Shtrikman bounds represent the end-member scenarios for perfectly connected pores (HS+) and isolated pores (HS–):

$$\sigma_{\text{HS-}} = \sigma_s + \varphi \left(\frac{1}{\sigma_f - \sigma_s} + \frac{1 - \varphi}{3\sigma_s} \right)^{-1} \quad (8)$$

$$\sigma_{\text{HS+}} = \sigma_f + (1 - \varphi) \left(\frac{1}{\sigma_s - \sigma_f} + \frac{\varphi}{3\sigma_f} \right)^{-1} \quad (9)$$

The thickness of the surface sedimentary layer has a primary control on the frequency required to penetrate to basement. Figure 3 shows the influence of sedimentary thickness on the MT response function, in this case exemplified by the invariant phase derived from the phase tensor approach (Caldwell et al. 2004). In this example, a $10 \text{ } \Omega \text{ m}$ sedimentary cover of varying thickness overlies a $500 \text{ } \Omega \text{ m}$ basement. Increasing thickness of the sediments pushes the minima in the phase curve, a proxy for the sediment/basement contact, from about 0.1 s to about 5 s, for a sediment thickness from 150 to 1000 m,

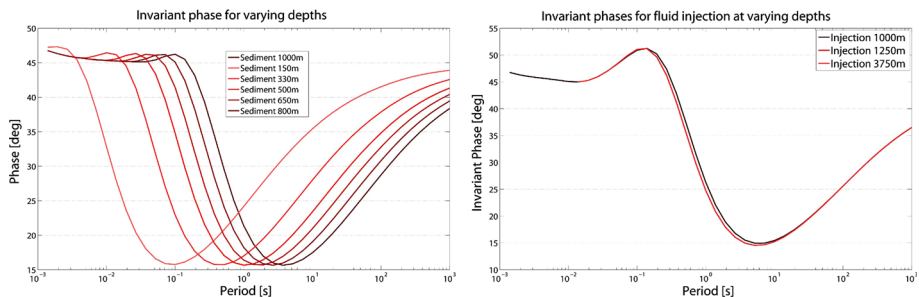


Fig. 3 The influence of a sedimentary layer on the MT transfer functions and resulting phases derived from 3D forward modeling (Mackie et al. 1993). Left: thickening of sediments from 150 to 1000 m shifts the phase tensor-derived invariant phase minimum (Caldwell et al. 2004) curve to longer periods from about 0.1 to about 5 s. The phase minimum represents the transition from conductive sediments ($10 \text{ } \Omega \text{ m}$) to resistive basement ($500 \text{ } \Omega \text{ m}$). Right: invariant phase curves for a fluid injection beneath 1 km of sediments with resistivity of $10 \text{ } \Omega \text{ m}$. The modeled fluid volume is $1 \times 1 \times 0.5 \text{ km}$ at resistivity of $3 \text{ } \Omega \text{ m}$. A significant separation between the sediments and the injected fluid is necessary to map a temporal change in the responses

respectively. This means resolution for a potential fluid injection must occur at much lower frequency in case of sediment thickness exceeding 1 km.

In order to minimize the screening effect of the layers overlying the fluid injection target depth, Ogaya et al. (2016) investigate the difficulties in monitoring changes at a synthetic CO₂ injection site using a layer stripping approach. While the authors investigate a CO₂ injection scenario, it is equally applicable to EGS, CGS, and TSG systems. Layer stripping relies on the 1D analytical solution for the propagating EM fields (Wait 1954) and removes the shielding effect of the overlying temporally static layers. As a result, the sensitivity to the fluid injection layer increases, within measurement error. The detectability is defined as the difference in the impedance tensor Z between pre- and post-injection, normalized by the error ε in the measurements.

$$D_{|Z|} = \frac{||Z_{\text{post}}| - |Z_{\text{pre}}||}{\sqrt{\varepsilon_{Z_{\text{pre}}}^2 + \varepsilon_{Z_{\text{post}}}^2}} \quad (10)$$

The value of $D_{|Z|}$ remains nearly constant for all layers above and within the CO₂ reservoir. However, while the detectability $D_{Z_{\text{real}}}$ of the real part are largest at the surface, the detectability of the imaginary part $D_{Z_{\text{imag}}}$, and the phase D_{ϕ} are largest near the depth of the CO₂ injection (Ogaya et al. 2016) and occur over a smaller period range (Fig. 4). This supports the analysis approaches focusing on the phase information using phase tensors on real time-lapse data sets (Peacock et al. 2012, 2013; MacFarlane et al. 2014), due to their

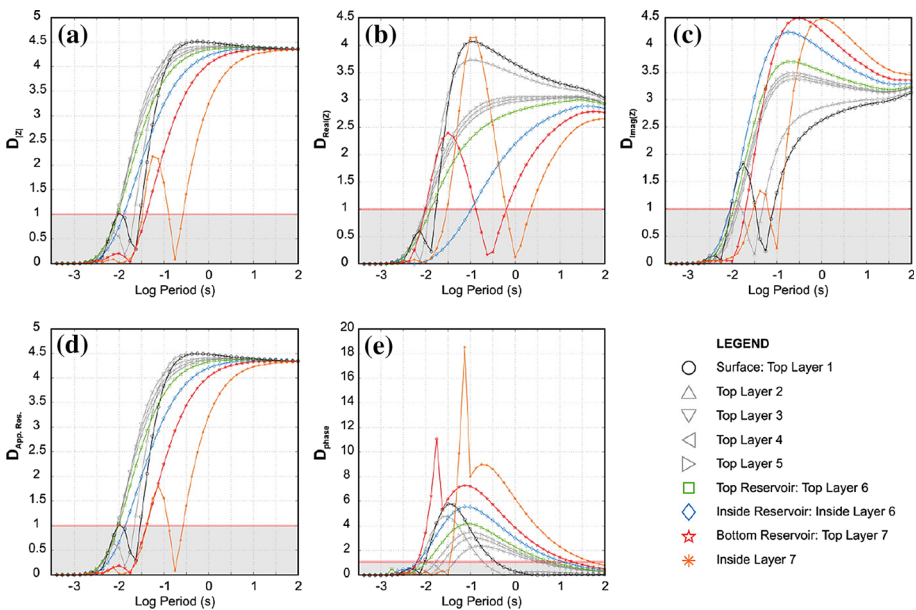


Fig. 4 Detectability values of a 20 Ωm plume at a depth of 800 m and extent $1700 \times 1700 \times 70 \text{ m}^3$ beneath a mostly 150 Ωm overburden covered with a sedimentary layer. **a** detectability of the absolute impedance tensor; **b** the real part of the impedance tensor; **c** the imaginary part of the impedance tensor; **d** the apparent resistivity; **e** the detectability of the phase. While the detectability of the real part and the apparent resistivity of the impedance tensor is largest at the surface of the earth as a result of the injection, the imaginary part of the impedance tensor and the phase are largest near the depth of the injection of a CO₂ plume. Taken from Ogaya et al. (2016)

derivative nature with respect to the real part of the impedance tensor and apparent resistivity (Weidelt 1972).

2.2 Quantification of Change in the Data Domain

While the above sections dealt with the EM sensitivity of fluid injection, real field examples require robust data representation and analysis to illustrate change in the data domain and address the distortion effects which may occur in the data. A straightforward approach is to plot apparent resistivity and phase curves pre- and post-injection and investigate departures from the baseline data (Peacock et al. 2013; Rees et al. 2016a). Inspection of Q_a and ϕ , derived from the impedance tensor, is intuitive and one can directly determine the period range in which change due to fracking occurs (Fig. 5). This can then be compared qualitatively with forward modeling results to determine the approximate depth of fluid injection. The shortcomings of this straightforward data representation are the influence of galvanic distortion (Groom and Bahr 1992; Bahr 1991; Bibby et al. 2005; McNeice and Jones 2001), static shift (Jones 1988; Pellerin and Hohmann 1990; Spitzer 2001; Ledo et al. 2002), and the lack of directional information inherently present for individual components of the impedance tensor.

For these reasons, the magnetotelluric phase tensor representation has been most commonly employed for MT monitoring (Peacock et al. 2012, 2013; Abdelfettah et al. 2018; MacFarlane et al. 2014). The real and imaginary part, X and Y , respectively, of the impedance tensor can be expressed as:

$$\Phi = X^{-1}Y, \quad (11)$$

defining the phase tensor Φ (Caldwell et al. 2004). This expression allows a distortion-free representation of the phase information in Z and is commonly displayed as an ellipse

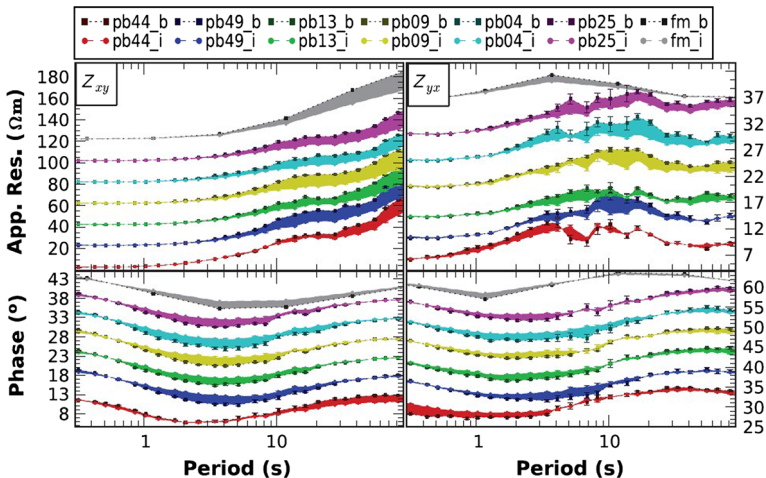


Fig. 5 Apparent resistivity and phase change for MT sites across the Paralana EGS within a 3 km radius (except pb44, located 7.5 km away and showing a smaller amplitude). Data responses pre-injection are denoted with subscript b and subscript i for post-injection responses. For comparison, the forward model responses are displayed in black and gray colors at the top of each sub-figure to illustrate the expected responses due to a fluid injection. Changes in phase occur at shorter periods compared to the apparent resistivity demonstrating the causality of change within the responses. Taken from Peacock et al. (2013)

(Abdelfettah et al. 2018; Peacock et al. 2012). More recently, studies have incorporated uncertainty into the calculation of phase tensors (Booker 2014) to assess the influence of noise on the measurements (Didana et al. 2017) (Fig. 6). For the purpose of monitoring change, the residual phase tensor is used to illustrate temporal changes for individual frequencies (Heise et al. 2008):

$$\Delta\Phi = I - \left(\Phi_{\text{pre}}^{-1} \Phi_{\text{post}} \right) \quad (12)$$

Figure 7 shows an example in which residual phase tensors are computed for a synthetic 3D forward model and compared with observed data across the Paralana EGS, South Australia (Peacock et al. 2013). The 3D forward model is constructed based on resistivity values derived from the baseline MT data, using a smooth 2D inversion code (de Groot Hedlin and Constable 1990). In addition to the assessment of the magnitude of change, the elliptical nature of the residual phase tensor allows for identification of directionality, i.e., which orientation experiences largest change. Figure 7, as an example across the Paralana EGS, South Australia, shows that MT sites close to the injection borehole have largest residual phase tensors with major axis oriented in a NNE direction coinciding with the NNE development of the microseismic cloud (see the corresponding Fig. 12 in the section on Case Studies).

A disadvantage of phase tensors is the lack of information on change in resistivity. Formulations exist which include this information, e.g., the resistivity tensors are able to show sign and magnitude of change but are prone to offsets and distortion in the electrical resistivity (Weckmann et al. 2003; Peacock et al. 2013) (Fig. 7). With the advent of new E-field loggers, which can be installed quickly and in large numbers across an injection site

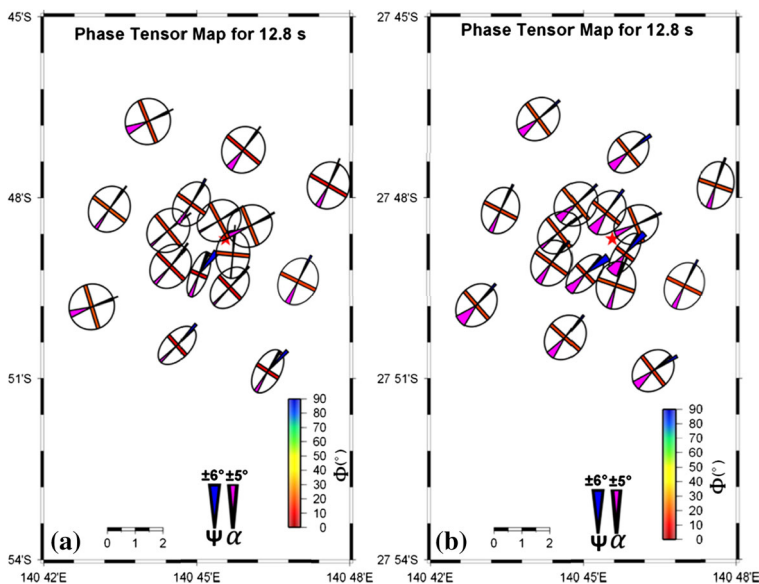


Fig. 6 Uncertainty phase tensor maps calculated from an ensemble of phase tensor components **a** pre-injection and **b** during injection. The phase tensor uncertainty maps are derived from observed impedance tensor plus random noise following (Booker 2014). This representation allows a better understanding of the influence of error on the direction and magnitude of change. Adapted from Didana et al. (2017)

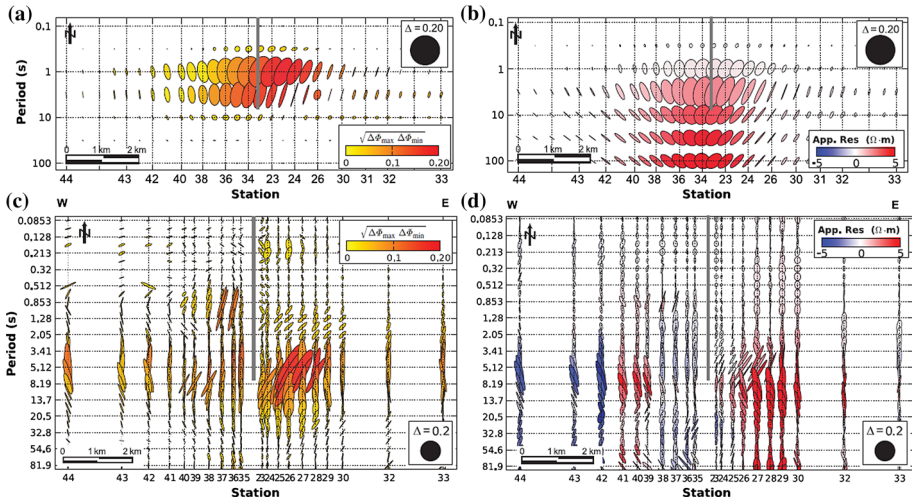


Fig. 7 Residual phase tensor (left column) and resistivity tensor (right column) pseudosection of the E-W profile across Paralana EGS. Top panel depicts residuals of 3D forward model with a conductive body of $0.3 \Omega\text{m}$ placed at 3.3 km depth with dimensions $1.5 \times 0.4 \times 0.8 \text{ km}$. Bottom row shows residuals derived from surface MT measurements of the fluid injection after (Peacock et al. 2013)

(Rees et al. 2016a), recent advances in inter-station transfer function in the form of an electric phase tensor representation appear promising (Bakker et al. 2015).

It should be noted that repeatability measurements are required for all time-lapse deployments that is analyzing temporal change prior to any fluid injection activity. This process will ensure that changes in the response functions are not due to natural source-related processes or other man-made influences, such as pipeline, generator, or train noise.

2.3 Quantification of Change in the Model Domain

Once changes in the EM field are identified in the data domain, the ultimate goal is to translate these changes to depth in order to map extent of the fluid fracking into the surrounding host rock. There are obvious constraints, as the depth of the fluid injection is known around the perforated borehole. However, the extent of the fracture network is governed by preexisting fracture networks and the regional stress field guiding the direction of rock failures due to the pressure of the stimulation. Additionally, electromagnetic monitoring has the potential to detect undesirable fluid leakage in shallower layers, for example as a result of cracks in the borehole casing.

Most studies, which ultimately seek to measure EM response changes, perform forward modeling to ascertain the sensitivity to the known target depth at which fluids are injected, in order to ascertain detectability of the extent of the fluid injection. To this end, forward modeling studies involve 1D studies which are somewhat limited in their value due to the unrealistic infinite extent of conductors at the location fluid injection (Rees et al. 2016a). More realistic results are expected from 3D forward modeling using background resistivity obtained from 2D/3D inversion models of the sediments and basement (Peacock et al. 2013; Tietze et al. 2015; Didana et al. 2017). A comparative analysis between a model with and without a 3D volume representing the injected fluid then provides insight into the expected change in magnitude of surface time-lapse EM measurements. Figure 8 illustrates

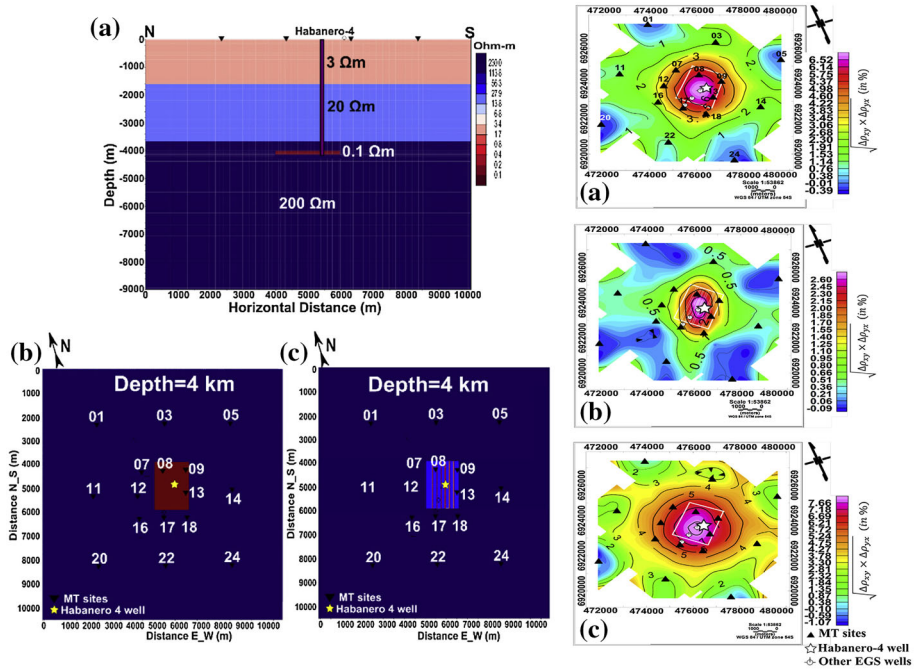


Fig. 8 3D MT forward modeling of a $0.1 \Omega \text{m}$ body at 4 km representing the fluid injection volume. The background 1D model is informed by 2D inversions representing conductive sediments overlying a resistive basement. Right-hand side shows apparent resistivity change measured at surface for **a** maximum 6.7% difference for isotropic $0.1 \Omega \text{m}$ body; **b** maximum 2.7% difference for anisotropic $0.1 \Omega \text{m}$ body; and **c** maximum 8% difference when changing the top sedimentary layer from 3 to $10 \Omega \text{m}$ for an isotropic body at depth. Adapted from Didana et al. (2017)

one such example for which a fluid injection at a depth of 4000 m results in a maximum of 6.7% change in apparent resistivity at the surface, given an isotropic $0.1 \Omega \text{m}$ fluid volume in a $400 \Omega \text{m}$ background resistivity and a layered sedimentary package at surface gradually increasing in resistivity (Didana et al. 2017). If the fluid volume is anisotropic, with a preferred orientation for fluid connection and therefore electrical conductivity, the surface apparent resistivity change reduces by more than 50%. An increase in the magnitude of change can be expected if the sediment resistivity increases as a result of the reduction in the screening effect of the sedimentary layer compared to when its resistivity would be lower.

Virtual experiments highlight the significance of optimal survey design to ensure sensors are placed where maximum change is likely to occur in EM responses. In particular, borehole measurements are vastly superior in detecting subtle conductivity enhancements due to fluid injection (Börner et al. 2015a, b; Streich et al. 2010; Tietze et al. 2015).

The inverse problem of relating subtle measurement perturbations due to fluid injection to a resistivity image proves more difficult due to the non-uniqueness and diffuse nature of electromagnetic methods. Examples include modeling of temporal changes in the space domain using deterministic 1D inversions (Didana et al. 2017), probabilistic 1D inversions (Rosas-Carbajal et al. 2015), deterministic 2D inversions (Didana et al. 2016; Rees et al. 2016b), and deterministic and probabilistic 3D inversions (Rosas-Carbajal et al. 2015).

Numerous studies have used 2D smooth inversion codes (de Groot Hedlin and Constable 1990; Key 2016; Rodi and Mackie 2001) to invert for change of profiles or individual sites in the vicinity of the perforated drillhole (Rees et al. 2016a, b; Didana et al. 2017). A straightforward strategy is to invert a profile of MT sites with responses pre- and post-injection and calculate the difference of the resistivity models. In the case displayed in Fig. 9, the difference in resistivity exceeds 20% at a depth of 2.5 km and is readily visible.

A second approach using 2D inverse codes is to invert a ‘profile’ of individual station responses calculated from different times during the deployment. Didana et al. (2017), for example, use 24-h windows to calculate the MT transfer function, which are then modeled using the 2D inversion algorithm MARE2DEM (Key and Ovall 2011). The motivation for this approach is twofold. Firstly, the inversion process allows an estimate of the depth of change, and secondly the model norm of the inversion acts as a filter to random noise. However, this temporal 2D inversion approach is still a rather qualitative way of translating changes measured at the surface to depth.

Given the small changes in the transfer function and the influence of noise, arguably the future for inverting for changes is using probabilistic inversions. Rosas-Carbajal et al. (2015) illustrate that deterministic 3D smooth inversion algorithms result in poorly constrained depth estimates for change. The study primarily used the off-diagonal phase data of the time-lapse responses across the Paralana EGS, South Australia, due to larger variations in the apparent resistivity estimates, to invert for 3D resistivity structure prior to and after injection using the smooth 3D inversion algorithm ModEM (Egbert and Kelbert 2012; Kelbert et al. 2014). The deterministic 3D inversion placed the largest reduction in resistivity at 700 m, and not at 3700 m where the injection occurred.

To achieve a better depth estimate, Rosas-Carbajal et al. (2015) use a probabilistic 3D Markov chain Monte Carlo (MCMC) inversion of the time-lapse MT data, with the aim of calculating the posterior probability density function (pdf) of the model parameters. An advantage of probabilistic methods is the ability to address nonlinear relationships between data and model correctly, successful convergence to the posterior pdf, and to characterize parameter uncertainty (Sambridge and Mosegaard 2002). In the case of the time-lapse MT data, the temporal changes are derived from an initial 3D deterministic resistivity model. The injected fluid volume is characterized by a reduced Legendre moment decomposition,

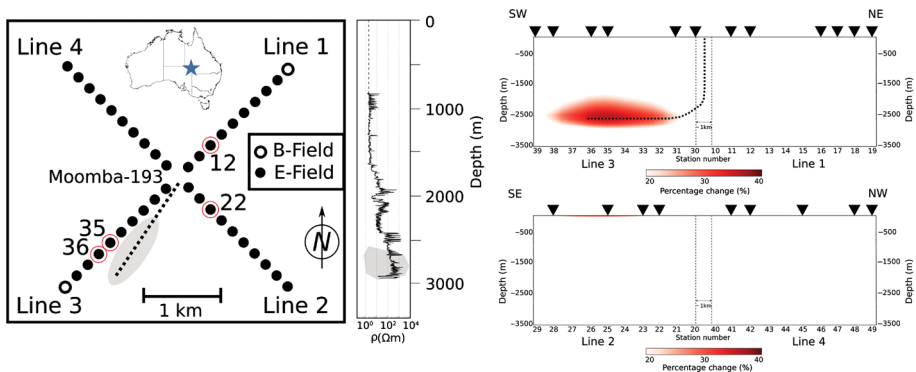


Fig. 9 Temporal resistivity change along 4 profiles using *B*- and *E*-field loggers for shale gas frack monitoring in the Cooper Basin, South Australia. The dotted line shows the direction of the horizontal Moomba 193 well and its resistivity log (left). Changes below 20% were cut off and not displayed. Adapted from Rees et al. (2016a)

relying on petrophysical relationships to save computational time. Legendre moments are geometrical moments which are typically used to describe geological or geophysical plumes, which make this representation suitable for the developing fluid fracture at depth. The Legendre parametrization by Rosas-Carbajal et al. (2015) is based on work by Laloy et al. (2012), who characterized an injected water plume in partially saturated media using inversions of synthetic crosshole ground-penetrating radar traveltime data, allowing a lower-dimensional model parameterization with less computational requirements. The plume can be described using the zero-order moment measuring the total mass, the first-order moments describing the center of mass, the second-order moments parameterizing the spread, and higher-order moments characterizing the morphological features of the plumes. A similar approach has been tried in MT inversions to represent conductivity structure as blobs representing a departure from an initial half-space resistivity (Alexander et al. 2012).

Figure 10 shows the posterior pdf of the injected volume at depth. The depth and spread of the volume tracer were well reproduced with a north–south extension as imaged with the microseismic event cloud. Nevertheless, the authors report that the petrophysical relationships were not able to explain the large resistivity changes inferred from the posterior pdf. Possible explanations could be the dependence on the smoothly varying baseline resistivity model and that the highly fractured network at depth is near percolation threshold and established enhanced connection upon fluid injection.

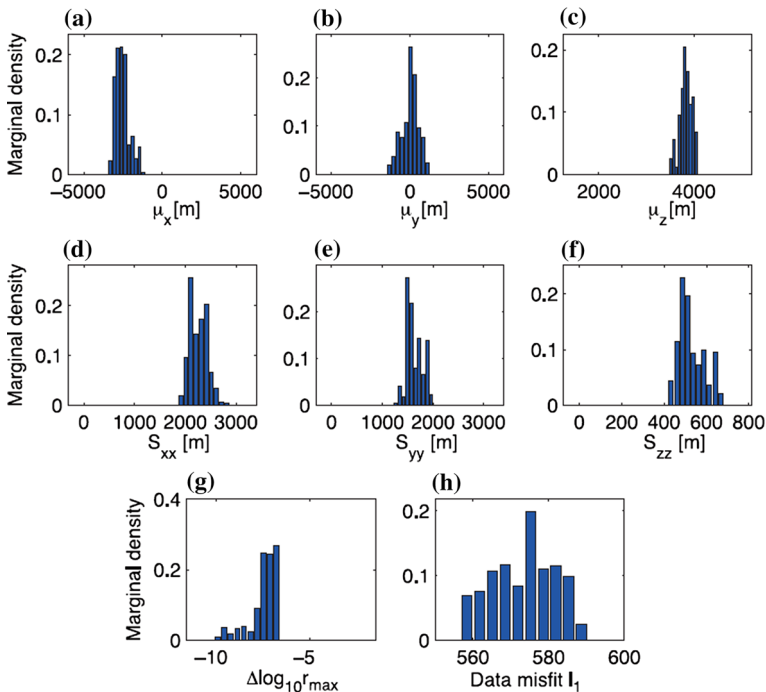


Fig. 10 Marginal posterior distribution of the center of mass (a–c), and center of spread (d–f) of the fluid injection plume at Paralana EGS. The maximum resistivity change and data misfit distribution is shown in (g) and (h), respectively. Adapted from Rosas-Carbajal et al. (2015)

3 Case Studies

3.1 Fluid Fracking in Geothermal Areas

3.1.1 Paralana EGS

Fluid fracking in enhanced geothermal systems typically occurs at depths of around 4 km to access sufficient temperatures of 200 °C required to achieve economic viability for electricity generation. The Paralana EGS, South Australia, is arguably the most studied EGS worldwide for monitoring fluid fracking using EM methods in deep-seated EGS (Peacock et al. 2012, 2013; MacFarlane et al. 2014; Rosas-Carbajal et al. 2015; Alexander et al. 2012; Albaric et al. 2014). The area is characterized by anomalously high heat flow across the wider area of the Flinders Ranges as part of the South Australian Heat Flow anomaly (Neumann et al. 2000). The elevated heat flow ($> 90 \text{ mW m}^{-2}$) is attributed to high abundance of U and Th in the Proterozoic granites of the Mt. Painter Inlier basement (Brugger et al. 2005). The Paralana EGS is approximately 10 km east of the Flinders Ranges comprising the Mt. Painter Inlier. Here, the heat-trapping sedimentary blanket reaches depths of over 3.5 km (Table 1). However, baseline MT profiles indicate that sediments are electrically conductive only to about 1 km (Thiel et al. 2016). The far-field stress acting upon the Flinders Ranges lead to enhanced seismicity (Balfour et al. 2015), elevated heat flow (Neumann et al. 2000; Holford et al. 2011), and metamorphic devolatilization reactions in the lower to mid-crust resulting in heterogeneous conductivity structure in the crustal column (Thiel et al. 2016).

Within this geological setting, Petratherm Limited established an EGS site to the east of the Flinders Ranges, South Australia, in the Frome Embayment (Fig. 12). The chosen locality promised to have the necessary ingredients for a successful EGS, namely high heat flow and a thick insulating sedimentary blanket to trap the heat of the granites below the cover. Seismic reflection profiles across the Paralana EGS indicated fractures at the base of the sedimentary cover penetrating into the granitic basement. The preexisting higher density of fractures was seen to be beneficial to establish a fracture network open to fluid flow at the depth of the fluid injection. In July 2011, Petratherm Ltd. injected 3100 m³ of saline water into Mesoproterozoic metasedimentary rocks over a period of 4 days at a depth of 3680 m within the 4012-m-deep Paralana 2 drillhole. The drillhole was cased to 3750 m depth and perforation occurred over a depth interval of 6 m.

Microseismic monitoring stations were employed as the conventional monitoring tool for fluid injections. The fluid injection caused more than 7000 microearthquakes with the largest amplitude in the vicinity of M_w 2.4–2.5 (Albaric et al. 2014). The microseismic cloud developed in a NNE–SSW direction and was interpreted to have focused on pre-existing fractures in the vicinity of the injection well (Fig. 11). While the microseismic monitoring is the conventional monitoring tool for fluid fracturing, its sensitivity to fracture development in the form of microearthquakes does not necessarily imply fluid propagation and connectedness. It is for these reasons that MT has been trialled as a monitoring tool at the Paralana EGS.

Following the discussion in the previous section of this manuscript on sensitivity considerations for fluid fracking, extensive forward modeling was undertaken prior to the injection. 2D inversion models of profiles across the injection site were used to populate a 3D forward model consisting of a layered subsurface. The top layer of 1 km thickness with 5 Ωm resistivity represents the sedimentary cover underlain another 1-km-thick layer (10

Table 1 Overview of field studies of electromagnetic monitoring for enhanced geothermal systems (EGS), coal seam gas (CSG), tight shale gas (TSG), and CO₂ storage sites

Location	Target	Type of study	References
Paralana (Australia)	EGS	Characterization, continuous and time-lapse monitoring, anisotropy modeling, probabilistic inversion (MT, microseismics)	Peacock et al. (2012), Peacock et al. (2013), MacFarlane et al. (2014), Rosas-Carbajal et al. (2015) and Thiel et al. (2016)
Habanero (Australia)	EGS	Characterization, continuous and time-lapse monitoring (MT)	Didana et al. (2017)
Rittershofen (France)	EGS	Continuous monitoring (MT)	Abdelfettah et al. (2018)
Cooper Basin (Australia)	TSG	Continuous monitoring (MT)	Rees et al. (2016a, c)
Surat Basin (Australia)	CSG	Continuous monitoring (MT)	Rees et al. (2016b, c)
Otway Basin (Australia)	EGS	Characterization and anisotropic inversions (MT)	Kirkby et al. (2015)
Thailand oil fields	Oil	Characterization including anisotropy, surface to borehole CSEM, well log constraint, seismic integration	Strack et al., pers.comm.
Newberry (USA)	EGS	Characterization (MT)	Newman, pers.comm.
Gross Schoenebeck (Germany)	EGS	Characterization (MT, seismic)	Muñoz et al. (2010b, a)
Ketzin (Germany), Hontomin (Spain)	CO ₂	Characterization	Grayver et al. (2014), Ogaya et al. (2013) and Börner et al. (2015b)
Bockstedt (Germany)	Oil	Characterization, modeling studies, surface to borehole CSEM	Tietze et al. (2015)

Ω m), a 1.5-km layer of 200 Ω m, a 500-m layer of 70 Ω m, and a more resistive quarter space of 500 Ω m dipping toward the east, and representing the granitic basement of the Flinders Ranges and Mt. Painter Inlier. At 3.3 km depth, a 0.3 Ω m block with dimensions of 1.5 km \times 0.4 km \times 0.8 km represented the fluid injection volume. Three-dimensional forward modeling using the code of Mackie et al. (1993) between the model with and without the conductive block resulted in an 8% change in the predicted surface apparent resistivity variation, suggesting that observing change due to a fluid injection is feasible for the lithology at the Paralana EGS site (Peacock et al. 2013).

Two types of deployments were undertaken, a continuous and time-lapse deployment to monitor the fluid injection using MT. During the continuous deployment, eleven broadband MT sites were placed around the borehole, measuring throughout the entire fluid fracturing (Peacock et al. 2012). While the continuous deployment is arguably the preferred method, it is limited by the availability of instrumentation. For this reason, a second method of time-lapse monitoring was tried which involves the deployment of an array of sites larger than the number of instruments available before and after the fluid injection. In the case of the Paralana EGS, time-lapse monitoring involved the deployment of 56 MT sites around

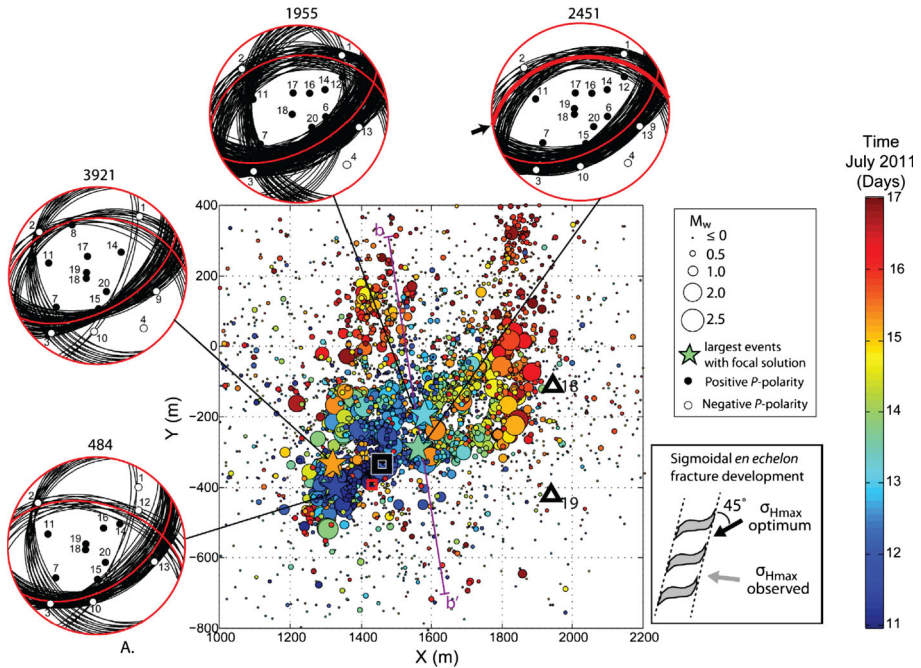


Fig. 11 Map view of microseismicity recorded during the fluid injection period at Paralana EGS in July 2011. The microseismic cloud developed from the injection well (black rectangle) outward along an interpreted en echelon fault system (right hand diagram) in the NNE–SSW direction. Blue colors represent microseismic events at commencement of fluid injection, and redder colors denote events associated with the end of the fracturing (15th July) and the two consecutive days. The focal solutions are presented for the four largest earthquake events with acceptable and preferred mechanisms in black and red lines, respectively. Adapted from Albaric et al. (2014)

the injection hole before and after the fracking (Peacock et al. 2013) (Fig. 12). The two types were designed to establish the suitability for monitoring the fracking given that practical considerations, such as instrumentation or temporal access to the site, may be a limiting factor in future monitoring exercises.

The site spacing in both types of deployment was chosen based on the variation in surface MT response changes derived from 3D forward modeling. The continuous deployment during the fracking had 11 sites within a few hundred meters around the borehole up to a maximum distance of 2 km (Peacock et al. 2012). The layout of the time-lapse deployment consisted of 56 sites along two main orthogonal profiles of approximately 15 km length, with variable site spacing of 200 m near the borehole extending to 1.5 km toward the margins. Two shorter profiles at a 45° angle with 6 stations each provided some out-of-profile constraint. The entire site layout was aligned with the geoelectric strike of $N9^\circ E$, which was derived from phase tensor analysis and invariant analysis of the impedance tensor Z (Caldwell et al. 2004; Weaver et al. 2000).

A total of four pre-injection surveys were performed to obtain high-quality responses and assess repeatability of measurement in the case *without* a fluid injection. Due to local gas pipeline noise, only two of the four pre-injection measurements were used for repeatability analysis. Galvanic distortion due to local electric charge accumulations can

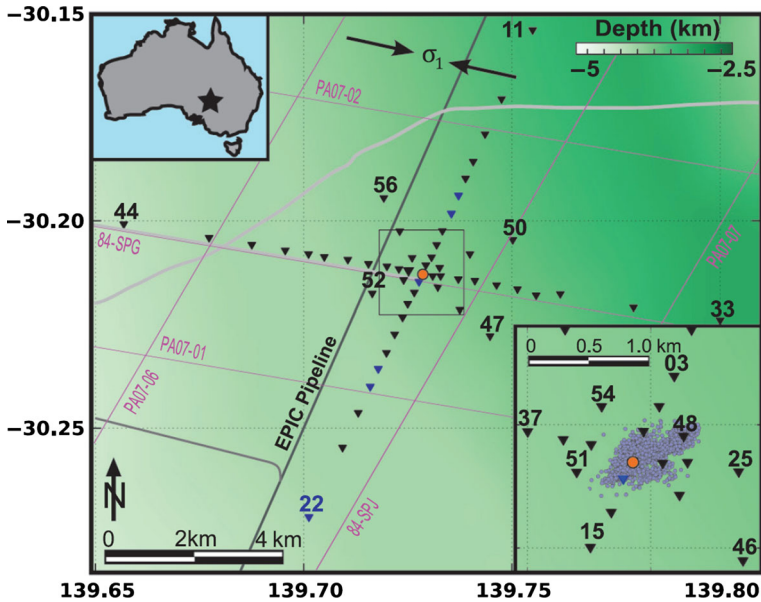


Fig. 12 Survey layout of the broadband MT sites (triangles) across the 3.7-km-deep borehole (red circle) of the Paralana EGS, South Australia. Inset shows microseismic events recorded during fracking (Albaric et al. 2014). Background color is depth to basement, and arrows denote maximum stress direction (Balfour et al. 2015). Lines show roads, seismic lines, and gas pipeline after (Peacock et al. 2013)

change the apparent resistivity behavior; therefore, the distortion-free phase tensor representation was used to gauge repeatability. The change in measurements between surveys prior to the injection was less than 1%.

A week after the fluid injection in July 2011, the grid as outlined in Fig. 12, was repeated to record possible surface response changes due to the injected fluid. Cultural noise was lower than during pre-injection surveys and 47 stations recorded high-quality impedance tensor estimates to allow temporal analysis of the impedance tensor.

The fluid injection at the Paralana EGS led to a reduction in apparent resistivity by a few % for sites across the survey in response to the fluid injection (Peacock et al. 2013) (Fig. 5). The change was causal in that it occurred both in the apparent resistivity and phase in the period range between 1 and 10 s, matching the expected period range deduced from 3D forward modeling using subsurface resistivities measured from the baseline survey. In particular, sites to the northeast of the injection well recorded largest change predominantly in the Z_{xy} component with smaller changes in the Z_{yx} component of the impedance tensor. This would suggest a better connection for electrical current flow in the NNE direction of the injected fluid volume. In order to suppress noise and influence of galvanic distortion, residuals were analyzed using the phase tensor and resistivity tensor approach (Caldwell et al. 2004; Weckmann et al. 2003).

Residual phase tensors also indicate that change is not isotropic, but oriented in a NNE direction aligning perpendicular to the maximum horizontal stress direction (Balfour et al. 2015) and parallel to existing fault systems. The results were further supported by coincident microseismic monitoring, indicating a preferred NE orientation of the seismic cloud and derived focal mechanisms of major seismic events (Albaric et al. 2014). At a period of around 8 s, the largest change of about 20% was observed between pre- and post-injection.

The response changes require a larger volume of fluid-filled rock matrix post-injection than would be anticipated from the 3100 m³ fluid injected into the porous rock matrix. A possible explanation may be the increased connectivity of existing fluids at target depths, which have connected under the influence of the injection pressure over a larger area than can be accounted for by the volume of the injection fluid within a porous matrix alone.

Subsequent studies support that small-scale fractures at depth are preferentially aligned and can be explained by anisotropic conductivity enhancement with surface measurements (MacFarlane et al. 2014). The anisotropic analysis followed on from the directional observation of the change reported in Peacock et al. (2012) and Peacock et al. (2013). The authors employed a two-dimensional forward modeling code to assign an anisotropic conductivity structure to the 1-km-wide injection volume at a depth of 4 km. While the study was able to replicate the strong directionality of the response changes from 2D anisotropic forward modeling, the ellipticity (the ratio of the maximum to minimum phase) of the residual phase tensors comparing the pre-injection to post-injection responses could not be readily reproduced. It shows that this study was able to highlight the importance of anisotropic modeling to represent small-scale fracture networks at depth. However, the 2D forward modeling approach chosen may not suffice to account for the dimensionality of the injected fluid volume, in particular its finite extension in the direction out of profile. Future modeling attempts should focus on a full 3D MT inversion code with added anisotropy.

As outlined in Sect. 2.3, the response changes at the Paralana EGS were inverted using a probabilistic 3D time-lapse inversion (Rosas-Carbajal et al. 2015). While the authors did not account for anisotropy, the probabilistic nature of the inversion allows a statistical model assessment of the fluid plume extent. The probabilistic 3D time-lapse inversion of the measured time-lapse MT data also supported a conductive plume oriented in the general N-S direction beneath the injection site (Rosas-Carbajal et al. 2015).

3.1.2 Habanero EGS

Following on from success at the Paralana EGS, a time-lapse MT installation occurred at Habanero EGS, Cooper Basin, South Australia, in 2012 (Didana et al. 2017). Geotherm Ltd operated the most advanced EGS in Australia at the time with already four geothermal wells in place around 1000 km north of Adelaide. The area is also part of the South Australian Heat Flow anomaly, similar to the Paralana EGS. The Habanero EGS differs in its thicker sedimentary layer (up to 2 km thickness) overlying the fracture reservoir, which is about 400 m deeper than compared to the Paralana EGS. In November 2012, Geotherm Ltd injected 36500 m³ over 14 days into the hot granitic reservoir at 4077 m depth using a near-surface aquifer fluid of 13 Ω m resistivity at 25 °C. The target fracture zone at depth was a shallow WSW-dipping fracture of 10 m thickness, which had been intersected by all four geothermal wells.

During drilling, significant amounts of existing fluids were encountered at around 4000 m depth and under high pressure of about 34 MPa (Holl and Barton 2015). As a result, the fracking occurred with larger amounts of injection fluids of 36,500 m³. Tracer test analyses between geothermal wells Habanero 1 and Habanero 3 (560 m apart) and Habanero 4 (700 m from Habanero 1) showed a tracer recovery of 56 and 70%, respectively (Ayling et al. 2015). Similarly to the Paralana EGS, the maximum horizontal stress direction is $82^\circ \pm 5^\circ$ (Holl and Barton 2015).

The data were collected by Quantec Geoscience along two perpendicular profiles prior to the injection up to 20 km away from the injection site. The central 5 \times 5 km was

deployed as a grid of sites closer to the borehole for better coverage of changes immediately surrounding the injection well. This time-lapse deployment was repeated after the injection to map out any changes due to the enhanced reservoir. Seventeen sites were deployed during the injection using instruments of the University of Adelaide to record continuously during the injection in November 2012 as well (Didana et al. 2017). As expected, the responses showed a predominantly 1D behavior dominated by the horizontally layered sedimentary cover. There are slight splits in the apparent resistivity and phase curves between the orthogonal Z_{xy} and Z_{yx} components for periods longer than 100 s, suggesting a preferred fracture orientation. Strike analysis using invariant analysis and phase tensors (Weaver et al. 2000; Caldwell et al. 2004) indicated a strike of $N50^\circ E$ across the survey area.

Three-dimensional forward modeling of the fluid plume generated by the injection suggests small changes in the period band around 10 s given a three-layered resistivity distribution as discussed in Sect. 2.3 and shown in Fig. 8. The assigned resistivities of the 3D forward model were based on MARE2DEM 2D inversion (Key 2016) results derived from the orthogonal profiles across the Habanero EGS sites (Fig. 13). The fluid plume at depth with the extensions of $2.1 \times 1.5 \times 0.1$ km was assigned a resistivity of $0.1 \Omega m$ (Fig. 8). forward modeling predicted a 6.7 or 2.7% change depending whether the fluid volume was isotropic or anisotropic. The typical measurement errors on the apparent resistivity and phase were on the order of 1–2%.

The Habanero MT data showed an average decrease in apparent resistivity of about 5% for periods longer than 10 s. The decrease occurs predominantly in the NE direction perpendicular to the prevailing maximum horizontal stress. This behavior is comparable to the effects at the Paralana EGS. As outlined in Sect. 2.3, Didana et al. (2017) tried to translate the residual response changes of the impedance tensor between pre- and post-injection data into the model domain by inverting the pre-injection TE-mode data at one representative site (site 09 with E -field aligned with the orientation of maximum change) in 2D using the MARE2DEM 2D inversion code of Key (2016). Instead of inverting a spatial profile, the daily MT responses are lined up along a profile and inverted 'temporally' in 2D. A similar approach was undertaken by Rees et al. (2016b) (see also Fig. 14). The model reproduced a reduction in resistivity in the model domain; however, the smooth nature of

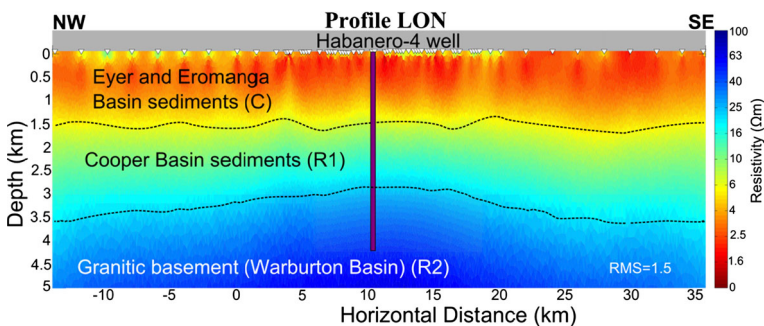


Fig. 13 2D inverse resistivity model of the EW MT profile across the Habanero EGS, Cooper Basin, South Australia, derived using the MARE2DEM 2D inverse code by Key (2016). The fluid injection occurred at a depth of 4077 m within the granite basement. The frack reservoir is overlain by the conductive Eyre and Eromanga sediments with less than $10 \Omega m$ resistivity and the more consolidated and resistive Cooper Basin sediments. Adapted from Didana et al. (2017)

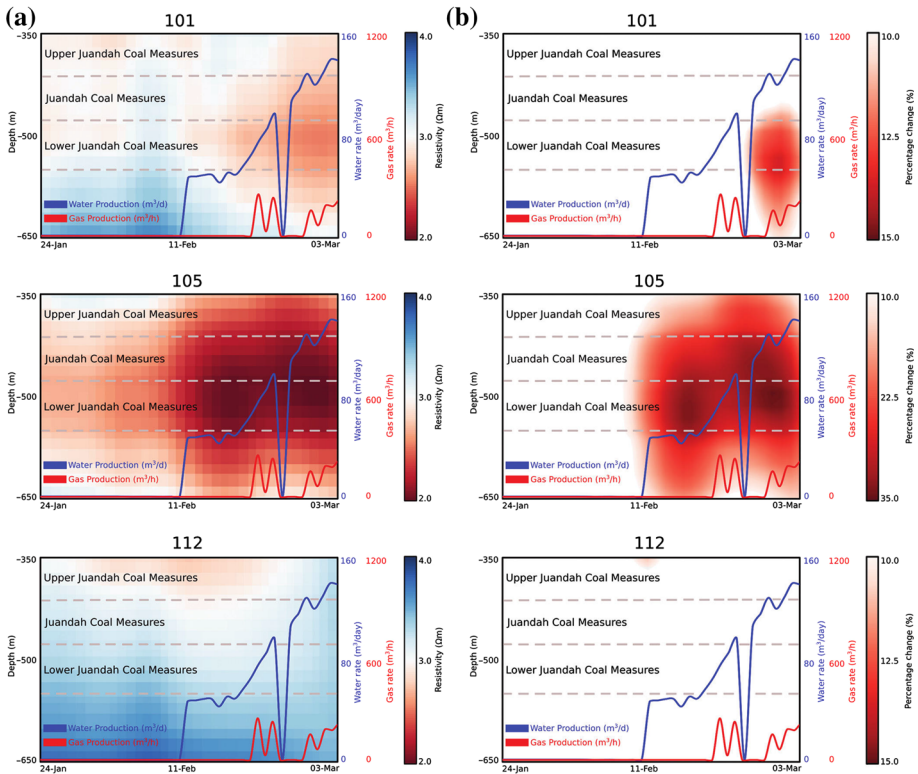


Fig. 14 **a** Time-lapse inversion showing the temporal variation in the target coal seam resistivity beneath individual sites along two orthogonal MT profiles. The blue line represents the water production rate (m^3/day), and the red line represents the gas production rate (m^3/h) from an injection well. **b** Percentage decrease in subsurface resistivity relative to the resistivity profile of the baseline data. Changes greater than 10% were considered significant. Three rows represented three MT stations 101, 105 and 112 along the east-west oriented profile in proximity to three production wells co-located along the E-W profile. Station 105 is closest to the well with highest water production rate and shows the largest change in resistivity due to the fracturing and subsequent water extraction. Adapted from Rees et al. (2016b)

the inversion smears the reduction in resistivity across a wide depth band from between 2 and 5 km.

3.1.3 Other EGS

Another recent type example involves time-lapse MT monitoring at five stations at the Rittershofen geothermal project, France, during a well flow test in 2014 (Abdelfettah et al. 2018). Five sites recorded for several months from June to December 2014 at a sampling rate of 512 Hz across the geothermal reservoir at depths of between 2.5 and 2.8 km. The data analysis largely followed the learnings from Peacock et al. (2012, 2013) and relied mainly on the phase tensor invariants [the maximum phase Φ_{\max} , $\Delta\Phi_{\max}$, $\Delta\Phi$, and the azimuth of the phase tensor ($\alpha - \beta$)] to analyze changes in the response functions during the continuous monitoring period. Abdelfettah et al. (2018) use the skin-depth relationship (Eq. 1) to infer that a fracturing-related observation should occur in the frequency range of

0.15–0.03 Hz. Changes in phase tensor properties occurred in the right period range predicted to represent the stimulated fracture network at depth. While two events coincided temporally with an acid and brine injection, there were other periodic (3–4 days) fluctuations, which have been attributed to possible tidal effects in the reservoir. Water table fluctuations were observed at the Soultz-sous-Forêts EGS in France due to tidal forces. However, further analysis is needed at the Rittershofen EGS to ascertain the changes are not noise related, as it could potentially be a bigger influence in a highly populated area, such as the Rhinegraben (Gérard et al. 2006), compared to the electromagnetically quiet Australian Outback.

The Newberry EGS, Oregon, USA, project began in 2011 with setup for monitoring an EGS stimulation at Newberry volcano in central Oregon in 2012 (A. Schultz, pers. comm). At that time, they combined 3-D/4-D MT, ground surface deformation (satellite InSAR and ground-based true aperture radar interferometry), with microgravity to observe the stimulation. Unfortunately, there was a technical problem with the stimulation, and rather than stimulating the EGS reservoir at 2000–3000 m below ground level, the fluid injection was too shallow (~ 600 m). There was a second stimulation (successful) in 2014, and a repeated monitoring effort began using ground deformation and MT. The data are still being processed at this stage and proved to be a challenging target. Only 9500 m^3 of pure water, no proppants, was used in the hydroshear. This was at 2000–3000 m depth in a primarily basalt–andesite volcanic complex, although there were also granitic intrusives. The microseismic cloud was quite tightly constrained to the vicinity of the well, with few microseismic events more than about 100 m radius distant.

3.2 Fluid Fracking in Hydrocarbon Plays and CO₂ Sequestration Scenarios

While there are many more fluid fracks occurring for shale gas and coal seam gas release around the world, EM monitoring studies of hydrocarbon fracks are scarcer than of geothermal examples. Fluid injection typically occurs at shallower depths, compared to geothermal EGS at around 2 km for tight shale gas and a few hundred meters for coal seam gas plays. Some early results exist for MT monitoring of coal seam gas extraction in Queensland, Australia (Rees et al. 2016b), and shale gas extraction in South Australia (Rees et al. 2016a) with an overview provided in (Rees et al. 2016c) (Fig. 14). In particular, coal seam pressurization is a related, yet different scenario to the geothermal fluid injections discussed above. The fluid frack and subsequent depressurization occur within the electrically conductive sediments. While an immediate increase in conductivity may be expected during the fracturing, the following depressurization may in fact increase resistivity as fluids are pumped back to the surface (Streich 2016). Rees et al. (2016b) performed a pilot MT monitoring study in the Surat Basin, Queensland, Australia, to monitor a CSG depressurization of coal beds at 500 ± 200 m depth containing interbedded clastic lithologies. The studies used a network of *E*-field loggers with just a few full MT instruments for rapid and expansive coverage of the injection area along two orthogonal profiles. Data processing followed the pseudo-remote reference processing approach of Muñoz and Ritter (2013). The observations showed a reduction in resistivity associated with the target coal seam formation of over 10% (Fig. 14). The reduction is attributed to a volume reduction following the sorptive gas release, which enhanced permeability of the coal seams (Mitra et al. 2012).

Similarly large changes in resistivity at target depth were observed for a shale gas frack in the Cooper basin, South Australia. The target depth in this case was at 2500 m (Rees

et al. 2016a). The larger than expected changes in electrical resistivity could not be attributed to the injected volume alone, but were interpreted to be from improved connectedness of the reservoir.

The CO₂ sequestration scenarios have received considerable attention in recent years, given the need to mitigate carbon emissions associated with hydrocarbon production (Randolph and Saar 2011). Studies span CO₂ site characterization using EM methods (Ogaya et al. 2013; Streich et al. 2010; Grayver et al. 2014; Börner et al. 2015b), laboratory measurements of the influence of CO₂ on electrical resistivity under reservoir temperatures and pressures (Börner et al. 2013), and inversion of CO₂ storage (Commer et al. 2016). These scenarios would typically cause a reduction in resistivity, and the high sensitivity of the MT method to conductors instead of resistors (Orange 1989) means that CO₂ sequestration sites stand a better chance for monitoring CO₂ movement using CSEM methods (Orange et al. 2009). A comprehensive review of CSEM for these applications is given in Streich (2016).

The change of the surface EM responses due to fluid injections leads to the question of what exactly is causing a reduction in resistivity. A logical explanation is that the injection of brine into the formation increases porosity and fluid saturation. However, in the cases described above, the changes in resistivity were too large to be simply explained by an addition of fluid.

4 Relationship of Fracking to Permeability

While the relationship between electrical resistivity of the formation and its porosity is relatively well understood, the fluid flow properties of an injected fluid are primarily dependent on the permeability k of the medium. Permeability can be divided into a primary formation permeability and a secondary permeability. The primary permeability is a function of interconnected pore space which has been reduced due to confining stress upon burial. Of particular interest during fracking is the introduction of fluid under pressure which enhances secondary permeability through establishing additional fractures along and around preexisting faults, most likely guided by regional stress. It is only the secondary permeability that will lead to sufficient flow rates to make EGS commercially viable. In comparison, conventional geothermal systems tend to have sufficient primary permeability for hot fluids to migrate to the surface when drilling has tapped the reservoir at depth.

It is difficult to map secondary permeability, as fractures are often only mm or cm thick and cannot be readily resolved using surface geophysical methods, such as seismic reflection (Bailey et al. 2014) or EM methods (MacFarlane et al. 2014). In addition, secondary permeability may be substantially controlled by fine-scaled distributed conduit systems rather than larger single faults (Caine et al. 1996).

Indications exist that secondary permeability is controlled by the regional stress field. One-dimensional anisotropic inversions of MT data across a geothermal area in the Otway Basin, Australia, revealed lowest bulk resistivity in a NNW direction with anisotropy ratios up to 100 (Kirkby et al. 2015). Fluid-filled fractures mapped using borehole permeability measurements across this area support the MT findings (Bailey et al. 2014). The general NNW-oriented fractures are favorably aligned for reactivation in the current horizontal stress field striking N125°E (Kirkby et al. 2015).

Similarly, secondary permeability created through fracking also appears to correlate with the direction of the regional stress field. Fluid injection at the Paralana EGS led to

biggest changes in MT responses in a NNE direction roughly perpendicular to the local compressive stress field with azimuth of $N96^\circ \pm 25^\circ E$ (Balfour et al. 2015). Figures 6 and 7 highlight the maximum phase tensor residual responses due to the injection for the Habanero and Paralana EGS, respectively. In both cases, the general orientation of the main phase tensor residual axis is in the NNE direction and is orthogonal to the regional stress field.

4.1 Laboratory Measurements of Permeability

One way to obtain estimates for permeability is via deriving porosity φ from bulk electrical conductivity σ using Archie's law (Archie 1942; Glover et al. 2000b; Glover 2010), e.g.,

$$\sigma = \sigma_f \varphi^m = \frac{\sigma_f}{F}, \quad (13)$$

whereby σ_f is the fluid conductivity in the fully saturated pores, F is the formation factor, defined as the ratio of the resistivity of the fluid-filled specimen to that of the pore fluid itself, and m is the cementation exponent (Glover 2009).

The inverse of the formation factor F is also known as the connectedness G , which is alternatively used in the literature to relate the fluid conductivity to the host rock conductivity. It is therefore a function of the porosity φ , e.g., $G \rightarrow 0$ if $\varphi \rightarrow 0$, and the connectivity χ of the pore space.

$$G = \varphi \chi \quad (14)$$

The cementation exponent on the other hand is interpreted as the rate of change of the connectedness with porosity and connectivity (Glover 2009):

$$m = \frac{d^2 G}{d\chi d\varphi} \quad (15)$$

Figure 15 illustrates the influence of the parameters controlling Archie's law on the electrical resistivity of the formation (Streich et al. 2010). If the temperature increases, the

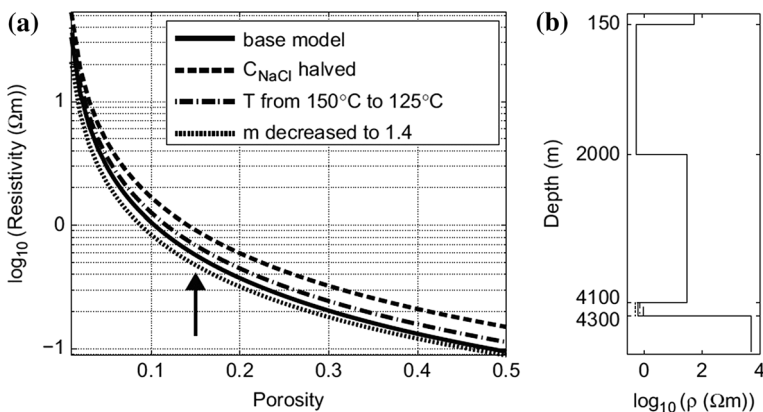


Fig. 15 Influence of parameters controlling the formation resistivity derived from Archie's law (Archie 1942). Starting from a fully saturated sandstone with 5.53 mol l^{-1} , plot a shows the effect of reducing the cementation factor m from 1.5 to 1.4 and reducing temperature of the formation. Adapted from Streich et al. (2010)

formation resistivity increases accordingly, while a decrease in the cementation factor m leads to an increase in electrical conductivity.

Archie's law is only applicable for a rock with a non-conducting matrix, and a modified form should be used if two conducting phases are present (e.g., fluid and matrix) (Glover et al. 2000a):

$$\sigma = \sigma_m \phi_m^p + \sigma_f \phi_f^m, \quad (16)$$

with σ_m being the matrix conductivity. Estimating permeability from porous media was originally based on capillary tube models. These assumptions work well for some scenarios, e.g., sedimentary basins, but have difficulties for other lithologies including clays (Thompson et al. 1987). The difficulties lie with the estimation of a hydraulic radius for a specific medium, as the pore volume-to-surface area ratio is not clearly defined for various formations.

It is inherently difficult to obtain absolute permeability estimates from geophysical measurements in the field either through borehole measurements and particularly for any type of surface geophysics deployment. Therefore, numerous studies have established empirical relationships to estimate permeability from a range of proxy measurements, which in most cases are measured downhole.

The permeability of a porous medium depends primarily on the porosity of the medium and its connectedness. The general form of the permeability equation can be written as:

$$k = \frac{GL^2}{c} \quad (17)$$

with a general length scale L (squared to achieve the unit for permeability in m^2 representing a measure for aperture), with G representing the connectedness, and c being a scaling constant which varies for different permeability models (Glover and Walker 2009). Using Eqs. 14 and 17 can be recast as:

$$k = \frac{\phi \chi L^2}{c} = \frac{\sigma_s L^2}{\sigma_f c}. \quad (18)$$

While Eq. 18 describes the general behavior of permeability, the plethora of empirical models in the literature has varying definitions of the length scales and varying constants. The variety of empirical models comprise two main types, the percolation (characteristic length scale) models and the Poiseuille-type models. It is beyond the scope of this article to provide a comprehensive overview of all the percolation and Poiseuille models for permeability estimation. Good reviews can be found in Walker and Glover (2010) and Rashid et al. (2015), showing the performance of these models on various rock types and bead packs.

The percolation models estimate the absolute permeability from the characteristic length scale L inherent to the rock type in question, typically the grain size, pore size, or pore throat size. The grain size and permeability can be determined using mercury injection capillary pressure (MICP) measurements in the laboratory or nuclear magnetic resonance (NMR) data downhole in the field (Glover et al. 2006).

MICP measurements provide the grain size spectra and are governed by the Washburn equation, which relates the capillary pressure P_c in a capillary tube of radius R to the interfacial tension of air and mercury $\nu_{\text{Hg-air}} = 0.48 \text{Nm}^{-1}$ and the wetting angle $\theta = 0^\circ$ (Washburn Mar 1921):

$$P_c = \frac{2\nu \cos \theta}{R} \quad (19)$$

As the sample is increasingly injected with mercury, a threshold pressure is reached when the saturation of mercury increases substantially. At this threshold point, the vast majority of porosity is filled and it represents the main fraction of porosity (Rashid et al. 2015).

The Schlumberger-Doll Research (SDR) model is the basic permeability prediction model used in conjunction with NMR measurements (Hidajat et al. 2004) and is defined as:

$$k_{\text{SDR}} = 4 \times 10^{-11} \varphi^4 T_{2\text{lm}}^2. \quad (20)$$

In this equation, $T_{2\text{lm}}$ denotes the logarithmic mean value of the NMR T_2 relaxation time in seconds.

Some examples of the permeability prediction models include the Kozeny–Carman (Schwartz et al. 1989), Katz and Thompson (1986; 1987), and RGPZ (Glover et al. 2006) models. Of these, the Kozeny–Carman model is deemed obsolete as it does not take into account the connectedness of the pores (Walker and Glover 2010). The Katz and Thompson model and the RGPZ model perform equally well on bead packs and rock cores of a sand-shale sequence in the UK (Walker and Glover 2010). The choice of which model to use in practical circumstances depends on the availability of fluid imbibition data or electrical data, in which case the Katz and Thompson or the RGPZ model is more appropriate, respectively (Walker and Glover 2010). As an example relationship for the percolation models, I show the permeability estimate of the RGPZ model (Glover et al. 2006):

$$k_{\text{RGPZ}} = \frac{d_{\text{grain}}^2}{4am^2 F(F-1)^2} \quad (21)$$

The grain size d_{grain} can be determined using MICP measurements, and its implementation is critical for the permeability estimation (Glover et al. 2006). The constant a usually takes the value $a = 8/3$.

The second class of models, the Poiseuille-type models, approximates the flow of a fluid through the rock with a bundle of tubes of varying diameter (Swanson 1981; Kolodzie 1980; Huet et al. 2005; Dastidar et al. 2007). Using scaling coefficients, the connectivity of the tubes is adjustable and can be matched to a specific rock type. Therefore, the Poiseuille-type models calculate the flow paths in the model in an exact manner as opposed to the percolation models (Rashid et al. 2015). Again, I demonstrate just one example for the Poiseuille-type models, following the Winland model as an example (Kolodzie 1980):

$$k_{\text{Winland}} = C_4 R_{35}^{a_2} \varphi^{a_3} \quad (22)$$

Here C_4 , a_2 , and a_3 are empirical values, and the radius R_{35} is calculated using the Washburn equation (Eq. 19) from the capillary pressure at a mercury saturation of 0.35.

From the two exemplary Eqs. 21 and 22 representing the Percolation and Poiseuille-type models, respectively, it becomes clear that the Poiseuille-type models require significant calibration, having often two or three empirical parameters. However, it should be noted that the calibration is always specific to a particular rock type and new calibration parameters have to be used in another formation.

4.2 Estimation of Permeability in the Field

The controlling factors for electrical conductivity and permeability can be thought of as similar. Both properties are partially controlled by the amount and the connectedness of pore space (Glover 2015). More recently, induced polarization (IP) measurements have been used to quantify surface area to pore volume through a power law relationship to the measured interfacial polarization. This approach together with new research form spectral induced polarization has advanced the estimation of interconnected surface area which ultimately controls fluid flow (Slater 2007). For the depths encountered for fluid fracking examples, near-surface IP measurements do not have the penetration depth required to image deep-seated fracking fluids at several hundred meters depth (Telford et al. 1976).

Attempts to estimate permeability from electrical resistivity measurements that are applicable to deep-probing EM techniques such as MT used a resistor network to replicate the bulk resistivity distribution at depth. Current pathways flow through a rectangular network of open resistors (representing open fractures) and closed resistors (electrically resistive matrix) (Bahr 1997). Due to the fractal nature of the resistor network, discrepancies between small anisotropic ratios from laboratory measurements and larger ratios obtained from field measurements could be explained. This highlights the importance of percolation threshold on the measured anisotropy ratios. While resistor networks link macroscopic anisotropy of electromagnetic measurements to in situ anisotropy, they do not provide a clear path to estimate hydraulic conductivity.

Bahr's resistor network only evaluated the bulk electrical conductivity of the medium and did not include estimation of fluid flow or variable resistance (Bahr 1997). Both hydraulic and electrical conductivity can be described by similar differential equations. Darcy's law describes hydraulic conductivity at low fluid velocities:

$$Q = -\frac{kA}{\mu} \nabla p \quad (23)$$

with Q is the volume flow rate, A is the cross-sectional area of the sample, μ is the fluid viscosity, and p is the fluid pressure. Ohm's law describes the equivalent electric current flow through the medium:

$$I = -\frac{A\sigma_f}{F} \nabla v \quad (24)$$

where I is the electric current, A is the cross-sectional area of the sample, and v is the electric potential or voltage. For simplified parallel plate models, it becomes apparent that hydraulic conductivity follows a cubic dependency on the fracture aperture b , whereas electrical conductivity is linearly proportional to b (Brown 1989). Deviations from the dependencies are expected in actual rock samples due to surface roughness and fractal behavior (Brown 1989; Ishibashi et al. 2015). As an example, fracture profiles from the Hachimantai hot dry rock test site, Japan, revealed a consistent fractal behavior for a range of scales from 0.01 to 40 mm (Glover and Hayashi 1997). However, Hagen–Poiseuille calculations of fluid transmissivity of synthetic fractures based on the fractal nature of the field observations overestimate the transmissivity by a factor of two. Glover et al. (1998a) conclude that the effect of rough surfaces needs to be taken into account for the synthetic fractures to match the field observations. One of the main reasons for the overestimation is the intrinsic behavior of fractures and specifically the rock fracture surfaces across a range of scales. The fracture surfaces show a strong correlation for long wavelengths, roughly a

few millimeters and above (Brown and Scholz 1986). However, at very short wavelengths the correlation is zero and the definition of the transition zone between the two end members controls the predictive behavior of the synthetic fracture models.

Figure 16 illustrates the progression of conceptual models over time to characterize the relationship between correlation of the fractures, also referred to as fracture matching, and the wavelength of fractures. Brown (1995) introduced a simple model for rough fractures which introduced a binary correlation coefficient (Fig. 16a) with a sudden cut-off threshold. Glover et al. (1998a, b) allowed a gradual linear change across the mismatch wavelength (ML in Fig. 16b), which still led to the overestimation of transmissivity of fluids as described above. Ogilvie et al. (2006) define a new fractal model with a mismatch wavelength, a transition length (TL) describing the transition zone between a minimum matching fraction (MFMIN) and a maximum matching fraction (MFMAX), and the shape of the function for the transition zone (Fig. 16c).

Given a matrix resistance R_m and fluid resistance R_f , a fracture resistance R_{frac} can be defined as:

$$\frac{\Delta z}{R_{\text{frac}}} = \frac{b}{R_f} + \frac{\Delta z - b}{R_m} \quad (25)$$

with Δz a fixed value representing the width of the fracture, and b the effective aperture of the fault.

Returning to scenarios involving fracture dilation and opening due to injected fluids under pressure, recent studies have investigated the dependency of matrix permeability as well as electrical conductivity on fracture aperture (Kirky et al. 2016). This scenario is crucial for understanding the changes from surface MT measurements which appear larger than model predictions by simple introduction of fluids into a volume (Rosas-Carbajal et al. 2015).

Figure 17 illustrates the conceptual behavior of permeability and electrical resistivity as fractures are opened. Zone 1 represents the base model scenario derived from baseline MT data prior to injection, an unfractured tight sedimentary rock or granite with isolated fluid pockets and small finite permeability and conductivity. Small separation between fracture surfaces results in small increases in k and σ , as most of the current and fluid pass through the matrix (primary permeability).

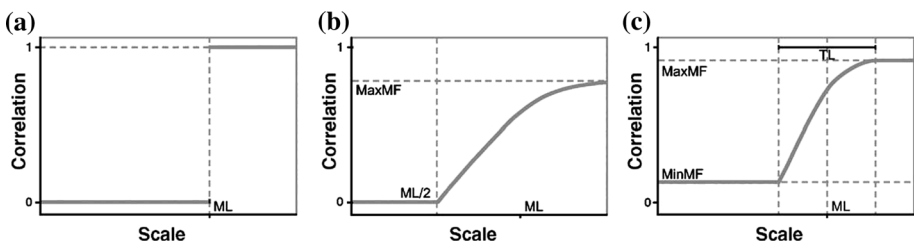


Fig. 16 Conceptual models describing the wavelength-dependent transition zone of fracture surface in rocks after (Ogilvie et al. 2006). **a** Early synthetic fracture models recognized that there exists no correlation between fracture surfaces for wavelength below a few millimeters (Brown 1995). **b** Glover et al. (1998a, b) introduced a gradual change across the mismatch wavelength (ML), resulting in improved fracture models. **c** With a definition of a transition length (TL) across the ML, from a minimum matching fraction (MFMIN) to a maximum matching fraction (MFMAX), Ogilvie et al. (2006) managed to achieve synthetic fracture models that accurately describe the fluid transmissivity for a variety of rock types resolving the overestimation of the model by Glover et al. (1998a, b)

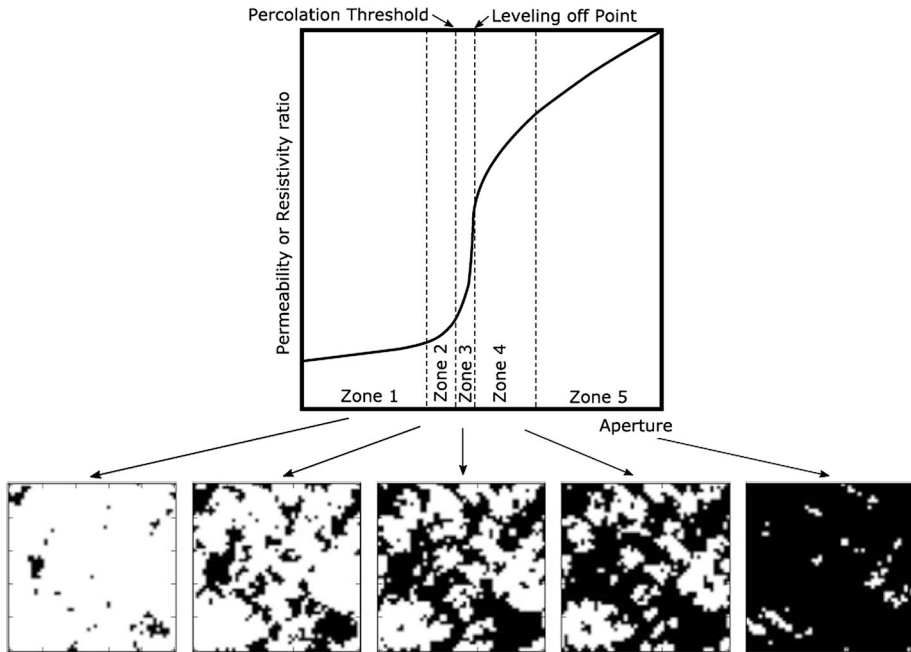


Fig. 17 Conceptual model based on an interpretation of the numerical results reported in Fig. 18 showing the behavior of permeability or resistivity as a function of separation of fracture surface after (Kirkby et al. 2016). Zones 1 and 2 show the lack of connectivity of the void spaces (black) within the rock matrix (white). As voids start to connect passing the percolation threshold, the permeability increases substantially. As the pore space continues to expand the increase in permeability levels off. At the same time the rate electrical resistivity reduction behaves in a similar fashion to the permeability

At the intersection between Zones 2 and 3 (Fig. 17), fractures are beginning to form a continuous fluid and current pathway at the point when the percolation threshold of the medium is achieved. Interestingly, the change in permeability and in the ratio between matrix and fracture electrical resistivity, defined as M , does not behave linearly (Fig. 18) across the small aperture change around the percolation threshold. Changes in M occur over a slightly wider range in aperture opening compared to permeability enhancement, which also carries a larger increase in log-space. Over a range of less than 0.01 mm in aperture opening, permeability can be enhanced by a factor of 10^4 , specifically for faults with small offset of 0.5 mm or less. M increases by a factor of 5 over the same mean aperture opening (Kirkby et al. 2016) for a model with a matrix permeability of 10^{-18} m^2 , and $m = 10^4$ (fluid to matrix resistivity).

The point at which the threshold occurs is characterized by a specific fracture to matrix resistivity value M_{PT} which is dependent on m following a power law relationship as follows (Kirkby et al. 2016):

$$M_{PT} = (0.38 \pm 0.02)m^{0.445 \pm 0.007} \quad (26)$$

Apart from the dependency on the fluid to matrix resistivity, the fracture-to-matrix resistivity ratio at the percolation threshold point M_{PT} also depends on fault offset (lateral shift of the fault surfaces) and fault spacing. Moderate offsets of 0.5 mm result in maximum values of M_{PT} for any ratio of fluid to matrix resistivity m compared to no offset or offsets

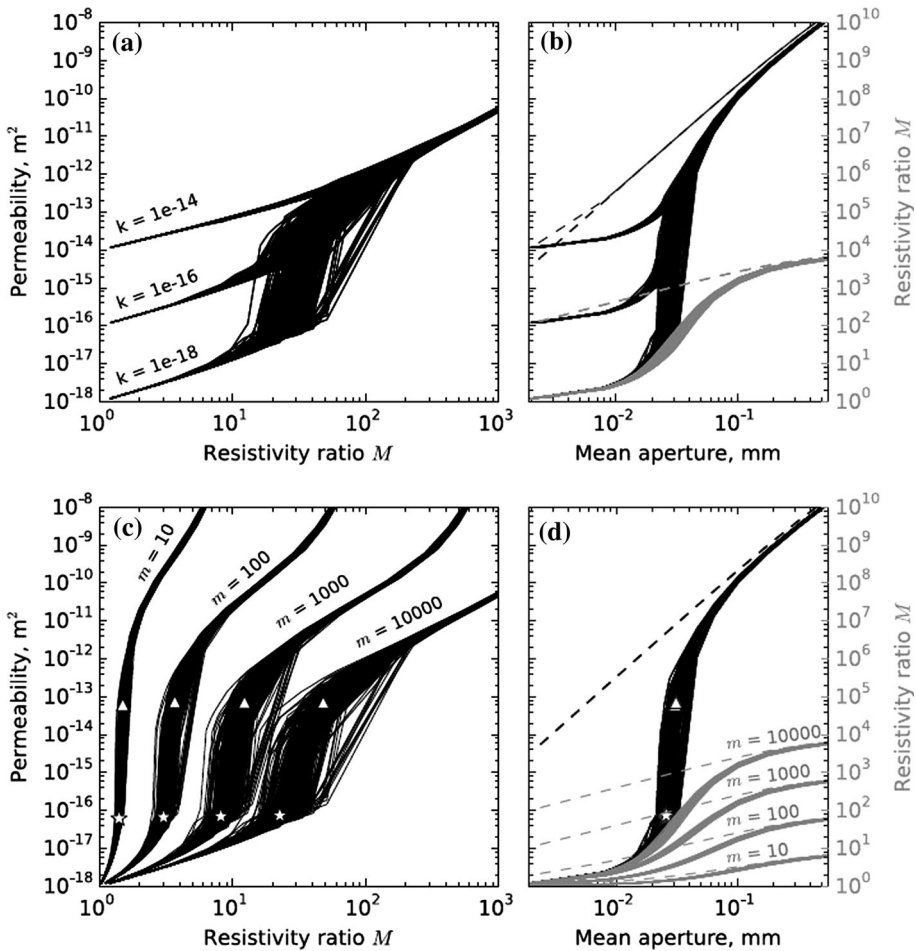


Fig. 18 Permeability k and rock-to-fracture resistivity ratio M during opening of fractures after (Kirkby et al. 2016). **a** k as a function of M for varying starting matrix permeability and **b** k and M as a function of arithmetic mean fracture aperture for $k = 10^{-14}, 10^{-16}, 10^{-18} \text{ m}^2$. **c** Permeability as a function of M for 4 different matrix to fluid resistivity ratios and **d** k and M as a function of arithmetic mean fracture aperture for $m = 10^1, 10^2, 10^3, 10^4$. Percolation threshold and leveling-off point indicated by stars and triangles, respectively

larger than about 1 mm (Kirkby et al. 2016). An increase in fault spacing on the other hand causes a reduction in permeability and the fracture-to-matrix resistivity ratio M_{PT} .

Once the mean fracture aperture reaches Zone 4 past the leveling-off point in the permeability and resistivity ratio, the curves approach values calculated by the parallel plate models (Brown 1989).

The significance of these findings is that transient stress enhancement due to the injection of fluids can increase fault spacing enough to bring the fracture network over the percolation threshold. For the purpose of surface measurements using EM methods, small changes in the mean aperture opening can increase the permeability as well as the fracture to matrix resistivity by several orders of magnitude. Quantitatively, the matrix-to-fracture resistivity ratio M_{PT} is in most cases less than 10; therefore, values greater than that should

indicate a fracture network that is above its percolation threshold and is therefore open to fluid flow (Kirkby et al. 2016). Resistivity ratios larger than 10 were used to forward model anisotropic changes in resistivity due to fluid injection at 4 km depth at Paralana EGS (MacFarlane et al. 2014) and estimated at between 2.5 and 3.5 km depth using 1D anisotropic inversions of MT data across the Koroit geothermal area in the Otway Basin, southeastern Australia (Kirkby et al. 2016). This suggests that the large resistivity ratios could be used to infer a favorable permeability allowing fluid flow in the enhanced fractures.

Kirkby and Heinson (2017) extended the resistor modeling to three dimensions showing the percolation behavior extends to a network of fractures from the single fracture behavior outlined in the previous paragraphs. The percolation of the fracture network depends largely on the density constant α , a fracture network property related to describe the power law relationship between fracture length, spacing, aperture, and displacement (Bonnet et al. 2001), and the separation of fracture planes.

One of the main insights from the 3D network modeling is the anisotropic behavior near the percolation threshold. Half of the fracture networks with a medium fracture density, e.g., $\alpha = 3$, displayed anisotropy even if all fractures were open due to the fact that the fracture network is near percolation threshold (Kirkby and Heinson 2017). Consequently, a fracture network with small fracture density, e.g., $\alpha = 0.3$, will never be open for fluid or electrical current flow as the fracture network itself is below the percolation point irrespective of the openness of the individual fractures. Dense networks, e.g., $\alpha = 30$, only show anisotropy if the individual fractures inside the network are near their percolation threshold. The network itself at that point is already above its own percolation threshold. Kirkby and Heinson (2017) report very strong anisotropy in these cases with ratios of up to 160 for resistivity and even up to 10^9 for permeability.

Given a rock permeability of 10^{-18} m² and a rock-to-fluid resistivity ratio of 10^4 in their study, Kirkby and Heinson (2017) report resistivity enhancements of up to 5000 and ten orders of magnitude permeability enhancements when the fracture network passes its percolation threshold. At the percolation threshold itself, small mean aperture changes of 0.02 mm can lead to 4 orders of magnitude permeability changes and a resistivity increase by a factor of 4.

In summary, the fracture network modeling and permeability estimations highlight the highly nonlinear behavior between fracture and network aperture versus permeability and electrical resistivity of the medium. The importance for EM monitoring of fracking is that the permeability modeling suggests a significant response function contrast during fracking, in particular if the reservoir at depth is below its percolation threshold prior to the injection and above the threshold after the injection. The monitoring studies have all indicated a strong directionality in the response changes with significant conductivity enhancement at depth. A possible explanation is therefore that the EM monitoring records a connection of fractures in an orientation roughly perpendicular to the maximum stress field. The anisotropic behavior observed from the 3D network modeling should therefore be observed with the tensorial character of the impedance tensor, e.g., with the help of phase tensor analysis or other robust impedance tensor representations. While microseismic monitoring maps the fracture opening via transient strain release mechanisms of microearthquakes, the EM monitoring could in fact inform about the enhancement of connectivity of the reservoir with relevance for the ability for fluids to flow through the reservoir.

5 Conclusions and Future Direction

- Electromagnetic monitoring has been employed across several fluid injection scenarios ranging from enhanced geothermal systems, coal seam gas and shale gas plays, and CO₂ storage sites. Results from case studies suggest that EM monitoring is a viable tool to detect changes in electrical resistivity of the fluid reservoir at depth with surface measurements.
- Changes in apparent resistivity and phase during fluid injection at several hundred meters to a few kilometers depth are small from surface-based MT measurements and often just above measurement error. Great care has to be taken in choosing low-noise environments if possible. Repeatability studies are crucial, as well as handling galvanic distortion and static offsets.
- Electromagnetic responses are directional in that preferred connection is a function of the current stress field. These can be mapped using the phase tensor approach (or other directional representations of the impedance tensor) to illustrate preferred orientation of current flow. Microseismic monitoring supports establishment of preferred fracture connection. Anisotropy modeling is a useful tool to model directional changes in resistivity.
- Limitations still exist in adequately mapping the horizontal fluid extent of the injection plume due to lack of sensitivity and the screening effect of sediments.
- Forward modeling of the reservoir, the host rock and overlying strata (sedimentary basins in most cases) are vital for ground-truthing observation, specifically predicting changes of EM responses in the correct period range.
- Further petrophysical studies are needed to explain fracture development and its influence on fluid flow and relation to electrical resistivity over time within the fracture network. The percolation threshold of a fracture network plays an important role for permeability enhancement of the reservoir. At the percolation threshold, the connectedness increases in a highly nonlinear fashion, and permeability and electrical conductivity are enhanced by several orders of magnitude.
- Downhole measurements performed closer to the fracture network would be a step change in improving our understanding of in situ processes during fluid injection. Modeling studies indicate a significant increase in sensitivity to target for borehole-to-borehole, or borehole-to-surface configurations. This would alleviate resolution of the fluid plume extent at depth.
- Continued investigation into fluid flow at depth allows better technical appraisal for fluid as an ideal extraction agent for geothermal energy. This will allow a more informed debate on respective advantages of fluids versus CO₂ as a working fluid. The highly reactive properties and enhanced mobility of CO₂ may be preferable for efficiency with the added benefits of using an injection site for ultimately sequestering CO₂ after geothermal energy extraction and producing a negative carbon footprint (Randolph and Saar 2011).

Acknowledgements I would like to thank Ian Ferguson, and the other members of the Program Committee of the 23rd EM Induction Workshop for giving me the opportunity to present this review. I would also like to acknowledge numerous colleagues I worked with on this problem over the years, in particular Jared Peacock, who performed the pioneering analyses on the Paralana EGS. Subsequently, Yohannes Didana, Alison Kirkby, Jake MacFarlane, Graham Heinson, and many others greatly furthered research in this field. The South Australian Center for Geothermal Energy Research, guided by Martin Hand, supported a fellowship throughout the first few years of the EM monitoring research. Australian geothermal companies

Petratherm Ltd and Geodynamics allowed access to their EGS plays, making this research possible in the first place. Paul Glover and an anonymous reviewer helped to improve this manuscript.

References

- Abdelfettah Y, Sailhac P, Larnier H, Matthey P-D, Schill E (2018) Continuous and time-lapse magnetotelluric monitoring of low volume injection at Rittershoffen geothermal project, northern Alsace–France. *Geothermics* 71:1–11
- Aizawa K, Ogawa Y, Ishido T (2009) Groundwater flow and hydrothermal systems within volcanic edifices: delineation by electric self-potential and magnetotellurics. *J Geophys Res* 114:B01208
- Albaric J, Oye V, Langet N, Hasting M, Lecomte I, Iranpour K, Messeiller M, Reid P (2014) Monitoring of induced seismicity during the first geothermal reservoir stimulation at Paralana, Australia. *Geothermics* 52:120–131
- Alexander B, Thiel S, Peacock J (2012) Application of evolutionary methods to 3D geoscience modelling. In: Proceedings of the fourteenth international conference on genetic and evolutionary computation conference, GECCO '12, New York, NY, USA. ACM, pp 1039–1046. ISBN 978-1-4503-1177-9
- Archie GE (1942) The electrical resistivity log as an aid in determining some reservoir characteristics. *Trans AIME* 146:54–62
- Árnason K, Eysteinnsson H, Hersir GP (2010) Joint 1D inversion of TEM and MT data and 3D inversion of MT data in the Hengill area, SW Iceland. *Geothermics* 39(1):13–34
- Athy L (1930) Density, porosity, and compaction of sedimentary rocks. *AAPG Bull* 14:1–24
- Ayling BF, Hogarth RA, Rose PE (2015) Tracer testing at the Habanero EGS site, central Australia. In: World geothermal congress, Melbourne, Australia, p 10
- Bahr K (1991) Geological noise in magnetotelluric data: a classification of distortion types. *Phys Earth Planet Inter* 66:24–38
- Bahr K (1997) Electrical anisotropy and conductivity distribution functions of fractal random networks and of the crust: the scale effect of connectivity. *Geophys J Int* 130:649–660
- Bailey A, King R, Holford S, Sage J, Backe G, Hand M (2014) Remote sensing of subsurface fractures in the Otway Basin, South Australia. *J Geophys Res Solid Earth* 119(8):6591–6612
- Bakker J, Kuvshinov A, Samrock F, Geraskin A, Pankratov O (2015) Introducing inter-site phase tensors to suppress galvanic distortion in the telluric method. *Earth Planets Space* 67(1):160
- Balfour NJ, Cummins PR, Pilia S, Love D (2015) Localization of intraplate deformation through fluid-assisted faulting in the lower-crust: the flinders ranges, South Australia. *Tectonophysics* 655:97–106
- Bauer K, Muñoz G, Moeck I (2012) Pattern recognition and lithological interpretation of collocated seismic and magnetotelluric models using self-organizing maps. *Geophys J Int* 189(2):984–998
- Bertrand EA, Caldwell TG, Hill GJ, Bennie SL, Soengkono S (2013) Magnetotelluric imaging of the Ohaaki geothermal system, New Zealand: implications for locating basement permeability. *J Volcanol Geotherm Res* 268:36–45
- Bibby HM, Caldwell TG, Brown C (2005) Determinable and non-determinable parameters of galvanic distortion in magnetotellurics. *Geophys J Int* 163:915–930
- Bonnet E, Bour O, Odling NE, Davy P, Main I, Cowie P, Berkowitz B (2001) Scaling of fracture systems in geological media. *Rev Geophys* 39(3):347–383
- Booker JR (2014) The magnetotelluric phase tensor: a critical review. *Surv Geophys* 35(1):7–40
- Börner JH, Herdegen V, Repke J-U, Spitzer K (2013) The impact of CO₂ on the electrical properties of water bearing porous media—laboratory experiments with respect to carbon capture and storage. *Geophys Prospect* 61:446–460
- Börner JH, Bär M, Spitzer K (2015a) Electromagnetic methods for exploration and monitoring of enhanced geothermal systems: a virtual experiment. *Geothermics* 55:78–87
- Börner JH, Wang F, Weißflog J, Bär M, Görz I, Spitzer K (2015b) Multi-method virtual electromagnetic experiments for developing suitable monitoring designs: a fictitious CO₂ sequestration scenario in Northern Germany. *Geophys Prospect* 63(6):1430–1449
- Brown SR (1989) Transport of fluid and electric current through a single fracture. *J Geophys Res Solid Earth* 94(B7):9429–9438
- Brown SR (1995) Simple mathematical model of a rough fracture. *J Geophys Res Solid Earth* 100(B4):5941–5952
- Brown SR, Scholz CH (1986) Closure of rock joints. *J Geophys Res* 91(B5):4939
- Brugger J, Long N, McPhail DC, Plimer I (2005) An active amagmatic hydrothermal system: the Paralana hot springs, northern flinders ranges, South Australia. *Chem Geol* 222(1–2):35–64

- Cagniard L (1953) Basic theory of the magneto-telluric method of geophysical prospecting. *Geophysics* 18:605–635
- Caine JS, Evans JP, Forster CB (1996) Fault zone architecture and permeability structure. *Geology* 24(11):1025–1028
- Caldwell TG, Bibby HM, Brown C (2004) The magnetotelluric phase tensor. *Geophys J Int* 158:457–469
- Chave AD, Jones AG (2012) *The magnetotelluric method: theory and practice*. Cambridge University Press, Cambridge
- Chesworth W (ed) (2008) *Encyclopedia of soil science*. Springer, Netherlands
- Commer M, Newman GA (2009) Three-dimensional controlled-source electromagnetic and magnetotelluric joint inversion. *Geophys J Int* 178(3):1305–1316
- Commer M, Doetsch J, Dafflon B, Yuxin W, Daley TM, Hubbard SS (2016) Time-lapse 3-D electrical resistance tomography inversion for crosswell monitoring of dissolved and supercritical CO₂ flow at two field sites: Escatawpa and Cranfield, Mississippi, USA. *Int J Greenhouse Gas Control* 49:297–311
- Constable S, Weiss CJ (2006) Mapping thin resistors and hydrocarbons with marine EM methods: insights from 1D modeling. *Geophysics* 71:G43–G51
- Constable S, Key K, Lewis L (2009) Mapping offshore sedimentary structure using electromagnetic methods and terrain effects in marine magnetotelluric data. *Geophys J Int* 176(2):431–442
- Dastidar R, Sondergeld CH, Rai CS (2007) An improved empirical permeability estimator from mercury injection for tight clastic rocks. *Petrophysics* 48(3)
- de Groot Hedlin C, Constable S (1990) Occam's inversion to generate smooth, two-dimensional models from magnetotelluric data. *Geophysics* 55:1613–1624
- Didana YL, Thiel S, Heinson G (2014) Magnetotelluric imaging of upper crustal partial melt at Tendaho graben in Afar, Ethiopia. *Geophys Res Lett* 41(9):3089–3095
- Didana YL, Thiel S, Heinson G (2015) Three dimensional conductivity model of the Tendaho high enthalpy geothermal field, NE Ethiopia. *J Volcanol Geotherm Res* 290:53–62
- Didana Y, Heinson G, Thiel S (2016) Magnetotelluric monitoring of hydraulic fracture stimulation at the Habanero Enhanced Geothermal System, Cooper Basin, South Australia. In: 23rd electromagnetic induction workshop, Chiang Mai, Thailand
- Didana YL, Heinson G, Thiel S, Krieger L (2017) Magnetotelluric monitoring of permeability enhancement at enhanced geothermal system project. *Geothermics* 66:23–38
- Egbert GD, Kelbert A (2012) Computational recipes for electromagnetic inverse problems. *Geophys J Int* 189(1):251–267
- Garg SK, Pritchett JW, Wannamaker PE, Combs J (2007) Characterization of geothermal reservoirs with electrical surveys: Beowawe geothermal field. *Geothermics* 36(6):487–517
- Genter A, Guillou-Frottier L, Feybesse JL, Nicol N, Dezayes C, Schwartz S (2003) Typology of potential hot fractured rock resources in Europe. *Geothermics* 32(46):701–710
- Geothermal Technologies Program (2008) An evaluation of enhanced geothermal systems technology. Technical report, U.S. Department of Energy (DoE)
- G erard A, Genter A, Kohl T, Lutz P, Rose P, Rummel F (2006) The deep enhanced geothermal system (EGS) project at Soultz-sous-For ets (Alsace, France). *Geothermics* 35(56):473–483
- Glover P (2009) What is the cementation exponent? A new interpretation. *Lead Edge* 28(1):82–85
- Glover PWJ (2010) A generalized Archie's law for n phases. *Geophysics* 75(6):E247–E265
- Glover PWJ (2015) Geophysical properties of the near surface earth: electrical properties. In: Schubert G (ed) *Treatise on geophysics*. Elsevier, Amsterdam, pp 89–137
- Glover PWJ, Hayashi K (1997) Modelling fluid flow in rough fractures: application to the Hachimantai geothermal HDR test site. *Phys Chem Earth* 22(1–2):5–11
- Glover PW, Walker E (2009) Grain-size to effective pore-size transformation derived from electrokinetic theory. *Geophysics* 74(1):E17–E29
- Glover PWJ, Matsuki K, Hikima R, Hayashi K (1998a) Fluid flow in synthetic rough fractures and application to the hachimantai geothermal hot dry rock test site. *J Geophys Res Solid Earth* 103(B5):9621–9635
- Glover PWJ, Matsuki K, Hikima R, Hayashi K (1998b) Synthetic rough fractures in rocks. *J Geophys Res Solid Earth* 103(B5):9609–9620
- Glover PWJ, Hole MJ, Pous J (2000a) A modified Archie's law for two conducting phases. *Earth Planet Sci Lett* 180(3–4):369–383
- Glover PWJ, Pous J, Queralt P, Muoz J-A, Liesa M, Hole MJ (2000b) Integrated two-dimensional lithospheric conductivity modelling in the pyrenees using field-scale and laboratory measurements. *Earth Planet Sci Lett* 178(1–2):59–72

- Glover PW, Zadjali II, Frew KA (2006) Permeability prediction from MICP and NMR data using an electrokinetic approach. *Geophysics* 71(4):F49–F60. doi:10.1190/1.2216930
- Goertz-Allmann BP, Goertz A, Wiemer S (2011) Stress drop variations of induced earthquakes at the Basel geothermal site. *Geophys Res Lett* 38(9):L09308
- Grayver AV, Streich R, Ritter O (2014) 3D inversion and resolution analysis of land-based CSEM data from the Ketzin CO₂ storage formation. *Geophysics* 79(2):E101–E114
- Groom RW, Bahr K (1992) Corrections for near surface effects: decomposition of the magnetotelluric impedance tensor and scaling corrections for regional resistivities: a tutorial. *Surv Geophys* 13:341–379
- Harinarayana T, Abdul Azeez KK, Murthy DN, Veeraswamy K, Eknath Rao SP, Manoj C, Naganjaneyulu K (2006) Exploration of geothermal structure in Puga geothermal field, Ladakh Himalayas, India by magnetotelluric studies. *J Appl Geophys* 58:280–295
- Hashin Z, Shtrikman S (1962) A variational approach to the theory of the effective magnetic permeability of multiphase materials. *J Appl Phys* 33(10):3125–3131
- He Z, Hu Z, Gao Y, He L, Meng C, Yang L (2015) Field test of monitoring gas reservoir development using time-lapse continuous electromagnetic profile method. *Geophysics* 80(2):WA127–WA134
- Heise W, Caldwell TG, Bibby HM, Bannister SC (2008) Three-dimensional modelling of magnetotelluric data from the Rotokawa geothermal field, Taupo Volcanic Zone, New Zealand. *Geophys J Int* 173(2):740–750
- Heise W, Caldwell TG, Bibby HM, Bennie SL (2010) Three-dimensional electrical resistivity image of magma beneath an active continental rift, Taupo Volcanic Zone, New Zealand. *Geophys Res Lett* 37(10):L10301
- Hidajat I, Mohanty KK, Flaum M, Hirasaki G (2004) Study of vuggy carbonates using NMR and X-ray CT scanning. *SPE Reserv Eval Eng* 7(05):365–377
- Holford SP, Hillis RR, Hand M, Sandiford M (2011) Thermal weakening localizes intraplate deformation along the southern Australian continental margin. *Earth Planet Sci Lett* 305:207–214
- Holl H, Barton C (2015) Habanero field-structure and state of stress. In: *Proceedings the world geothermal congress, Melbourne, Australia*, pp 19–25
- Huet CC, Rushing JA, Newsham KE, Blasingame TA (2005) A modified purcell/burdine model for estimating absolute permeability from mercury-injection capillary pressure data. In: *International petroleum technology conference*
- Ishibashi T, Watanabe N, Hirano N, Okamoto A, Tsuchiya N (2015) Beyond-laboratory-scale prediction for channeling flows through subsurface rock fractures with heterogeneous aperture distributions revealed by laboratory evaluation. *J Geophys Res Solid Earth* 120(1):106–124
- Jones AG (1988) Static shift of magnetotelluric data and its removal in a sedimentary basin environment. *Geophysics* 53:967–978
- Katz AJ, Thompson AH (1986) Quantitative prediction of permeability in porous rock. *Phys Rev B* 34(11):8179–8181
- Katz AJ, Thompson AH (1987) Prediction of rock electrical conductivity from mercury injection measurements. *J Geophys Res* 92(B1):599
- Kelbert A, Meqbel N, Egbert GD, Tandon K (2014) Modem: a modular system for inversion of electromagnetic geophysical data. *Comput Geosci* 66:40–53
- Key K (2016) MARE2dem: a 2-d inversion code for controlled-source electromagnetic and magnetotelluric data. *Geophys J Int* 207(1):571–588
- Key K, Ovall J (2011) A parallel goal-oriented adaptive finite element method for 2.5-d electromagnetic modelling. *Geophys J Int* 186(1):137–154
- Kirkby A, Heinson G (2017) Three-dimensional resistor network modeling of the resistivity and permeability of fractured rocks. *J Geophys Res Solid Earth* 122(4):2653–2669
- Kirkby A, Heinson G, Holford S, Thiel S (2015) Mapping fractures using 1d anisotropic modelling of magnetotelluric data: a case study from the Otway Basin, Victoria, Australia. *Geophys J Int* 201(3):1961–1976
- Kirkby A, Heinson G, Krieger L (2016) Relating permeability and electrical resistivity in fractures using random resistor network models. *J Geophys Res Solid Earth* 121(3):1546–1564
- Kolodzie S (1980) Analysis of pore throat size and use of the Waxman–Smits equation to determine OOIP in spindle field, Colorado. In: *SPE Annual technical conference and exhibition. Society of Petroleum Engineers*
- Kristinsdóttir LH, Flóvenz ÓG, Árnason K, Bruhn D, Milsch H, Spangenberg E, Kulenkampff J (2010) Electrical conductivity and P-wave velocity in rock samples from high-temperature Icelandic geothermal fields. *Geothermics* 39(1):94–105

- Laloy E, Linde N, Vrugt JA (2012) Mass conservative three-dimensional water tracer distribution from Markov chain Monte Carlo inversion of time-lapse ground-penetrating radar data. *Water Resour Res* 48(7):W07510
- Ledo J, Gabas A, Marcuello A (2002) Static shift levelling using geomagnetic transfer functions. *Earth Planets Space* 54:493–498
- Leroy P, Revil A (2004) A triple-layer model of the surface electrochemical properties of clay minerals. *J Colloid Interface Sci* 270(2):371–380
- Liddell M, Unsworth M, Pek J (2016) Magnetotelluric imaging of anisotropic crust near Fort McMurray, Alberta: implications for engineered geothermal system development. *Geophys J Int* 205(3):1365–1381
- MacFarlane J, Thiel S, Pek J, Peacock J, Heinson G (2014) Characterisation of induced fracture networks within an enhanced geothermal system using anisotropic electromagnetic modelling. *J Volcanol Geotherm Res* 288:1–7
- Mackie RL, Madden TR, Wannamaker PE (1993) Three-dimensional magnetotelluric modeling using difference equations—theory and comparisons to integral equation solutions. *Geophysics* 58:215–226
- McNeice GW, Jones AG (2001) Multisite, multifrequency tensor decomposition of magnetotelluric data. *Geophysics* 66:158–173
- Miensopust MP, Jones AG, Hersir GP, Vilhjmsson AM (2014) The Eyjafjallajökull volcanic system, Iceland: insights from electromagnetic measurements. *Geophys J Int* 199(2):1187–1204
- Mitra A, Harpalani S, Liu S (2012) Laboratory measurement and modeling of coal permeability with continued methane production: Part 1—laboratory results. *Fuel* 94:110–116
- Moorkamp M (2017) Integrating electromagnetic data with other geophysical observations for enhanced imaging of the earth. *Surv Geophys*. doi:10.1007/s10712-017-9413-7
- Muñoz G (2014) Exploring for geothermal resources with electromagnetic methods. *Surv Geophys* 35(1):101–122
- Muñoz G, Ritter O (2013) Pseudo-remote reference processing of magnetotelluric data: a fast and efficient data acquisition scheme for local arrays. *Geophys Prospect* 61:300–316
- Muñoz G, Ritter O, Moeck I (2010a) A target-oriented magnetotelluric inversion approach for characterizing the low enthalpy Groß Schönebeck geothermal reservoir. *Geophys J Int* 183(3):1199–1215
- Muñoz G, Bauer K, Moeck I, Schulze A, Ritter O (2010b) Exploring the Groß Schönebeck (Germany) geothermal site using a statistical joint interpretation of magnetotelluric and seismic tomography models. *Geothermics* 39(1):35–45
- Nesbitt BE (1993) Electrical resistivities of crustal fluids. *J Geophys Res* 98:4301–4310
- Neumann N, Sandiford M, Foden J (2000) Regional geochemistry and continental heat flow: implications for the origin of the South Australian heat flow anomaly. *Earth Planet Sci Lett* 183(1–2):107–120
- Ogaya X, Ledo J, Queralt P, Marcuello Á, Quínta A (2013) First geoelectrical image of the subsurface of the Hontomín site (Spain) for CO₂ geological storage: a magnetotelluric 2D characterization. *Int J Greenhouse Gas Control* 13:168–179
- Ogaya X, Ledo J, Queralt P, Jones AG, Marcuello Á (2016) A layer stripping approach for monitoring resistivity variations using surface magnetotelluric responses. *J Appl Geophys* 132:100–115
- Ogilvie SR, Isakov E, Glover PWJ (2006) Fluid flow through rough fractures in rocks. II: a new matching model for rough rock fractures. *Earth Planet Sci Lett* 241(34):454–465
- Orange AS (1989) Magnetotelluric exploration for hydrocarbons. *IEEE Proc* 77:287–317
- Orange A, Key K, Constable S (2009) The feasibility of reservoir monitoring using time-lapse marine CSEM. *Geophysics* 74(2):F21–F29
- Peacock JR, Thiel S, Reid P, Heinson G (2012) Magnetotelluric monitoring of a fluid injection: example from an enhanced geothermal system. *Geophys Res Lett* 39(18):L18403
- Peacock J, Thiel S, Heinson G, Reid P (2013) Time-lapse magnetotelluric monitoring of an enhanced geothermal system. *Geophysics* 78(3):B121–B130
- Pearson C (1981) The relationship between microseismicity and high pore pressures during hydraulic stimulation experiments in low permeability granitic rocks. *J Geophys Res Solid Earth* 86(B9):7855–7864
- Pellerin L, Hohmann GW (1990) Transient electromagnetic inversion: a remedy for magnetotelluric static shifts. *Geophysics* 55:1242–1250
- Phillips WS, Rutledge JT, House LS, Fehler MC (2002) Induced microearthquake patterns in hydrocarbon and geothermal reservoirs: six case studies. *Pure Appl Geophys* 159(1):345–369
- Pommier A (2014) Interpretation of magnetotelluric results using laboratory measurements. *Surv Geophys* 35(1):41–84
- Randolph JB, Saar MO (2011) Combining geothermal energy capture with geologic carbon dioxide sequestration. *Geophys Res Lett* 38(10):L10401

- Rashid F, Glover PWJ, Lorinczi P, Hussein D, Collier R, Lawrence J (2015) Permeability prediction in tight carbonate rocks using capillary pressure measurements. *Mar Pet Geol* 68:536–550. doi:[10.1016/j.marpetgeo.2015.10.005](https://doi.org/10.1016/j.marpetgeo.2015.10.005)
- Rees N, Carter S, Heinson G, Krieger L (2016a) Monitoring shale gas resources in the Cooper Basin using magnetotellurics. *Geophysics* 81(6):A13–A16
- Rees N, Heinson G, Krieger L (2016b) Magnetotelluric monitoring of coal seam gas depressurisation. *Geophysics* 81(6):E423–E432
- Rees N, Carter S, Heinson G, Krieger L, Conway D, Boren G, Matthews C (2016c) Magnetotelluric monitoring of coal-seam gas and shale-gas resource development in Australia. *Lead Edge* 35(1):64–70
- Rodi W, Mackie RL (2001) Nonlinear conjugate gradients algorithm for 2-D magnetotelluric inversion. *Geophysics* 66:174–187
- Rosas-Carbajal M, Linde N, Peacock J, Zyserman FI, Kalscheuer T, Thiel S (2015) Probabilistic 3-D time-lapse inversion of magnetotelluric data: application to an enhanced geothermal system. *Geophys J Int* 203(3):1946–1960
- Sambridge M, Mosegaard K (2002) Monte carlo methods in geophysical inverse problems. *Rev Geophys* 40(3):3-1–3-29
- Schwartz LM, Sen PN, Johnson DL (1989) Influence of rough surfaces on electrolytic conduction in porous media. *Phys Rev B* 40(4):2450–2458. doi:[10.1103/physrevb.40.2450](https://doi.org/10.1103/physrevb.40.2450)
- Slater L (2007) Near surface electrical characterization of hydraulic conductivity: from petrophysical properties to aquifer geometries: a review. *Surv Geophys* 28:169–197
- Spichak V, Manzella A (2009) Electromagnetic sounding of geothermal zones. *J Appl Geophys* 68(4):459–478
- Spitzer K (2001) Magnetotelluric static shift and direct current sensitivity. *Geophys J Int* 144:289–289
- Streich R (2016) Controlled-source electromagnetic approaches for hydrocarbon exploration and monitoring on land. *Surv Geophys* 37(1):47–80
- Streich R, Becken M (2011) Sensitivity of controlled-source electromagnetic fields in planarly layered media. *Geophys J Int* 187(2):705–728
- Streich R, Becken M, Ritter O (2010) Imaging of CO₂ storage sites, geothermal reservoirs, and gas shales using controlled-source magnetotellurics: modeling studies. *Chemie der Erde Geochemistry* 70:63–75
- Swanson BF (1981) A simple correlation between permeabilities and mercury capillary pressures. *J Pet Technol* 33(12):2498–2504. doi:[10.2118/8234-pa](https://doi.org/10.2118/8234-pa)
- Telford WM, Geldart LP, Sheriff RE, Keys DA (1976) Applied geophysics. Cambridge University Press, Cambridge
- Thiel S, Soeffky P, Krieger L, Regenauer-Lieb K, Peacock J, Heinson G (2016) Conductivity response to intraplate deformation: evidence for metamorphic devolatilization and crustal-scale fluid focusing. *Geophys Res Lett* 43(21):11,236–11,244
- Thompson AH, Katz AJ, Krohn CE (1987) The microgeometry and transport properties of sedimentary rock. *Adv Phys* 36(5):625–694
- Tietze K, Ritter O, Veeken P (2015) Controlled-source electromagnetic monitoring of reservoir oil saturation using a novel borehole-to-surface configuration. *Geophys Prospect* 63(6):1468–1490
- Tikhonov AN (1950) The determination of the electrical properties of deep layers of the Earth's crust. *Dokl Acad Nauk SSR* 73:295–297
- Uyeshima M (2007) EM monitoring of crustal processes including the use of the network-MT observations. *Surv Geophys* 28:199–237
- Vogt C, Kosack C, Marquart G (2012) Stochastic inversion of the tracer experiment of the enhanced geothermal system demonstration reservoir in Soultz-sous-Forêts: revealing pathways and estimating permeability distribution. *Geothermics* 42:1–12
- Wait JR (1954) On the relation between telluric currents and the earth's magnetic field. *Geophysics* 19:281–289
- Walker E, Glover PWJ (2010) Permeability models of porous media: characteristic length scales, scaling constants and time-dependent electrokinetic coupling. *Geophysics* 75(6):E235–E246
- Washburn EW (1921) The dynamics of capillary flow. *Phys Rev* 17(3):273–283. doi:[10.1103/physrev.17.273](https://doi.org/10.1103/physrev.17.273)
- Weaver JT, Agarwal AK, Lilley FEM (2000) Characterization of the magnetotelluric tensor in terms of its invariants. *Geophys J Int* 141:321–321
- Weckmann U, Ritter O, Haak V (2003) Images of the magnetotelluric apparent resistivity tensor. *Geophys J Int* 155(2):456–468
- Weidelt P (1972) The inverse problem of geomagnetic induction. *Zeitschrift fr Geophysik* 38:257–289
- Weidelt P (2007) Guided waves in marine CSEM. *Geophys J Int* 171(1):153–176